Toolbox for Quantum Computing With Spin Qubits

Jithesh Srinivas

A dissertation submitted in partial fulfillment

of the requirements for the degree of

Master of Philosophy

of

University College London.

Department of Physics & Astronomy

University College London

October 14, 2025

I, Jithesh Srinivas, confirm that the work presented in this thesis is my own. Where information has been derived from other sources, I confirm that this has been indicated in the work.

Contents

List of Figures

List of Tables

Abstract

Quantum computing fundamentally relies on the coherent evolution of two-level quantum states, known as qubits, to map input quantum states into output states. Such quantum systems have the potential to solve certain problems exponentially faster than classical computers. In this thesis, we develop a comprehensive electronic toolbox for the precise control and readout of charge- and spin-qubits hosted in solid-state Quantum Dots, particularly utilising carbon nanotube structures. This toolbox integrates sophisticated electrical instrumentation, including ultra-high-frequency quantum analysers, lock-in amplifiers, and high-bandwidth arbitrary waveform generators. A particular emphasis has been placed on developing the measurement sequencing for Rabi and Ramsey control pulses.

Impact Statement

Quantum computing represents one of the most transformative technological frontiers, with applications in cryptography, materials discovery, and artificial intelligence. This MPhil research has contributed to the development of an RF measurement toolbox for manipulating and measuring charge and spin qubits in carbon nanotube Double Quantum Dots (CNT-DQDs)—an emerging solid-state qubit platform known for its scalability.

Academic Impact

Within academia, this work advances methodologies for fast, high-fidelity control and readout of qubits. It demonstrates the integration of industry-grade instruments such as the Zurich UHF-QA/UHF-LI and Keysight M8195A with custom software automation, offering a practical blueprint for implementing low-latency feedback in cryogenic quantum experiments. The software driver developed for waveform upload and timing synchronisation enables scalable pulse-based control, which is critical for executing Rabi and Ramsey experiments. These contributions support experimental reproducibility and can be readily adopted by research groups working on Quantum Dot and microwave frequency instruments.

Additionally, the inclusion of simulation frameworks based on QuTiP and Qiskit for Rabi and Ramsey sequences provides a bridge between theoretical quantum dynamics and real-time hardware operation. These tools not only aid in interpreting experimental results but also inform

pulse calibration and decoherence analysis, enriching the curriculum for future quantum engineering education and training.

Societal and Industrial Impact

This research is also relevant to the broader quantum technology sector. The emphasis on carbon nanotube devices opens the door to leveraging materials with high mobility and strong spin-orbit coupling. The findings can inform the roadmap for the semiconductor industry for integrating quantum functionality into classical electronics.

The methods developed here also have the potential to benefit quantum instrumentation companies. The MATLAB driver written for the M8195A and the insights into signal distortion, latency, and rise/fall time mismatches can guide manufacturers in improving usability, timing precision, and user programmability of future quantum control hardware.

Impact Realisation Pathways

The dissemination of this work will occur through multiple channels:

- Contributions to peer-reviewed articles and upcoming collaborative publications on CNT Quantum Dots.
- Open-source release of the MATLAB driver and simulation scripts, facilitating reproducibility and wider adoption.
- Presentations at academic and industrial symposia, strengthening links between academic research and instrumentation developers.

By developing precise electronic control techniques, this project supports the scaling of spin-based quantum processors. Its impact will unfold incrementally through improved quantum experiment design, enhanced signal fidelity, and better informed qubit calibration protocols, advancing the field toward error-corrected and fault-tolerant quantum computation.

Glossary of Symbols

Symbol	Description
Ω_R	Rabi frequency, rate of coherent oscillation between two quantum states
T_{Rabi}	Rabi oscillation period, full cycle duration of qubit transition
T_2^{Rabi}	Coherence time extracted from Rabi decay
T_2^*	Effective coherence time / dephasing time due to noise
Q	Rabi quality factor, defined as T_2^{Rabi}/T_π
T_π	Duration of a π pulse (180° rotation in Bloch sphere)
$T_{\frac{\pi}{2}}$	Duration of a $\frac{\pi}{2}$ pulse (90° rotation)
Δ	Energy Detuning between drive frequency and qubit resonance
ω_d	Microwave drive frequency applied to qubit
ω_q	Qubit resonance frequency
γ	Decoherence rate, inverse of coherence time: $\gamma = 1/T_2$
A_{MW}	Amplitude of the Microwave Drive signal

Chapter 1

Introduction

Although quantum computing has recently gained public attention, the field of quantum computing and information has been around for several decades, dating back to the early theoretical models of quantum computation proposed in the 1980s [9], first proposed by Feynman [10] and Deutsch [11]. Later in the next decade, Peter Shor of AT&T's Bell Labs discovered Shor's algorithm [12], which allows quantum computers to factor large numbers much faster than existing algorithms. We now have the technology to create quantum chips with up to 128 qubits [13]. In this thesis, the practicality of Rabi and Ramsey experiments on a double Quantum Dot is demonstrated first through simulation, and then we discuss its implementation.

1.1 Fundamentals of Qubits and Gates

The fundamental information carrier in classical computing is a semiconductor transistor, with information-encoded states 0 and 1 determined by a current flow or none. Quantum computing uses quantum bits, also known as qubits, based on the quantum mechanical theory of superposition and entanglement. The superposition dictates that a qubit can exist in a superposition of logical $|0\rangle$ and $|1\rangle$ states, with probability amplitudes associated with each state, expressed as α and β (eq. 1.1, 1.2, 1.3), as a complex function. This probabilistic nature is better illustrated visually using the Bloch sphere model as seen in Figure 1.1.

$$|\psi\rangle = \alpha\,|0\rangle + \beta\,|1\rangle \tag{1.1}$$

$$|\psi\rangle = cos\frac{\theta}{2}|0\rangle + sin\frac{\theta}{2}e^{i\phi}|1\rangle \tag{1.2}$$

$$|\alpha|^2 + |\beta|^2 = 1 \tag{1.3}$$

A single qubit exists in a superposition of mixed states in the two-dimensional Hilbert space, and its state wavefunction $|\psi\rangle$ is expressed in the equation 1.2 by θ and ϕ: the polar and azimuthal angles, respectively. For a two-qubit system, each qubit has a measurement probability in the state 0 or 1 [1] and entanglement occurs to create a correlation between both qubit states; the quantum states can be represented by a density matrix $\rho = |\psi\rangle\langle\psi|$.

1.1.1 Quantum Gates

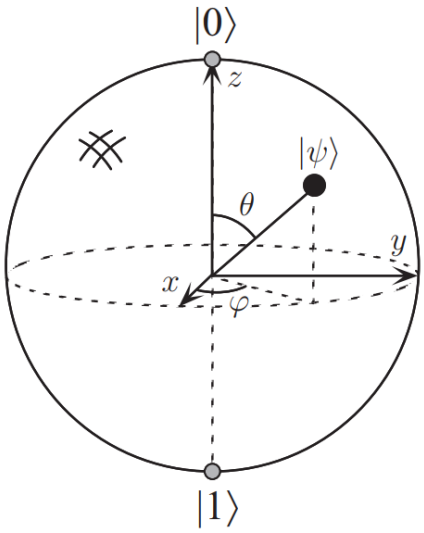

Figure 1.1: The Bloch sphere represents a single qubit state as a point defined by a polar angle θ and azimuthal angle φ, with axes corresponding to Pauli-$\mathbf{X},\mathbf{Y},\mathbf{Z}$ observables., [1]

A vector point $|\psi\rangle$ on the Bloch sphere (Fig. 1.1) represents the qubit state. A single-qubit gate is a rotation operation around the Bloch sphere in the (x,y,z) domain, and the Pauli matrices show rotation for each axis of the equation. 1.4 [1] [14]

$$\sigma_x = \begin{pmatrix} 0 & 1 \\ 1 & 0 \end{pmatrix}$$
$$\sigma_y = \begin{pmatrix} 0 & -i \\ i & 0 \end{pmatrix} \tag{1.4}$$
$$\sigma_z = \begin{pmatrix} 1 & 0 \\ 0 & -1 \end{pmatrix}$$

An electrical pulse induces a rotation around any axis and follows the rule that angles are additive. This qubit rotation can be expressed as matrices or in bra-ket notation (eq. 1.5) [1]. This thesis applies the rotation pulse through microwave signals to control the electron charge and spin properties, i.e., the qubit state. A standard qubit gate is the Identity Gate $\mathbf{I}$ that operates in a given input state $(\alpha|0\rangle + \beta|1\rangle)$ by multiplying with the identity operator $|0\rangle\langle 0| + |1\rangle\langle 1|$; equated in bra-ket or matrix form (1.6, 1.7).

$$\mathbf{I} = |0\rangle\langle 0| + |1\rangle\langle 1| \equiv \begin{pmatrix} 1 & 0 \\ 0 & 1 \end{pmatrix} \tag{1.5}$$

$$\begin{aligned} \mathbf{I}(\alpha|0\rangle + \beta|1\rangle) &= (|0\rangle\langle 0| + |1\rangle\langle 1|) \times (\alpha|0\rangle + \beta|1\rangle) \\ &= \alpha|0\rangle + \beta|1\rangle \end{aligned} \tag{1.6}$$

$$\mathbf{I}(\alpha|0\rangle + \beta|1\rangle) = \begin{pmatrix} 1 & 0 \\ 0 & 1 \end{pmatrix} \times \begin{pmatrix} \alpha \\ \beta \end{pmatrix} = \begin{pmatrix} \alpha \\ \beta \end{pmatrix} \tag{1.7}$$

A two-qubit system can occupy four logical states: $|00\rangle$, $|01\rangle$, $|10\rangle$, $|11\rangle$. Labeling the two qubits A and B, we can describe their quantum state ψ. The labels in bra-ket notation correspond to the state of that respective qubit in the formula, as seen in Eq. 1.8 which states all the possible states of the two-qubit system:

$$\psi = \alpha\,|00\rangle_{AB} + \beta\,|01\rangle_{AB} + \gamma|10\rangle_{AB} + \delta\,|11\rangle_{AB} \tag{1.8}$$

correspondingly, in matrix-vector form:

$$\begin{pmatrix} \alpha \\ \beta \\ \gamma \\ \delta \end{pmatrix} \tag{1.9}$$

where α, β, γ and δ are complex numbers and $|\alpha|^2 + |\beta|^2 + |\gamma|^2 + |\delta|^2 = 1$.

Another example of a gate operator is the two-qubit NOT gate. Its complete matrix derivation is provided in Appendix A.

1.2 Quantum Dots

In the context of double Quantum Dots, gates as **X** and **Y** correspond to physically tunable parameters such as tunnel coupling and detuning, while multi-qubit gates remain a future prospect. However, it is helpful to understand their formal construction.

1.2.1 Coulomb Blockade

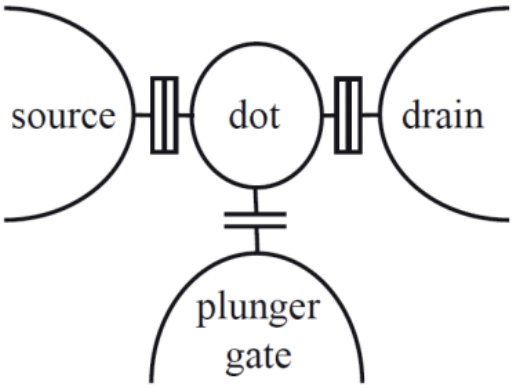

Figure 1.2: Example of a single electron transistor with the Quantum Dot connected to a source, drain, and plunger gate. [2]

The functioning of a single-electron transistor (SET) is based on the effect of the Coulomb blockade first reported in 1992 [15] [16]. A SET is similar to a

traditional MOSFET transistor, except instead of the channel, a conductive island called a Quantum Dot exists in this region with thin insulators separating the dot from the source and drain (quantum confinement), both being electron reservoirs. A single electron tunnels into the Quantum Dot from the source or drain by tuning a plunger gate electrode capacitively coupled to the dot island. Precise and nanoscale fabrication of the Quantum Dot material allows for regions with strong Coulomb repulsion, preventing free electron flow, known as the Coulomb blockade effect, and requires higher Coulomb energy [17].

$$E_C = \frac{e^2}{2C_\Sigma} \tag{1.10}$$

where E_C is the charging energy, and ΔE is the discrete orbital level spacing. In Figure 1.3, it is shown as the energy difference between the current occupied state and the next available empty state.

$$E_{addition} = E_C + \Delta E \tag{1.11}$$

where C_Σ is the total capacitance:

$$C_\Sigma = C_S + C_d + C_g \tag{1.12}$$

Adjusting the total electrochemical potential of the dot, we can provide E_C, the energy required for the transport of a single electron within the Quantum Dot. The charging energy E_C is defined in eq. 1.10 is related to C_Σ: the total capacitance of the source and drain junctions and the gate capacitor. This charging energy can also be represented in an energy level diagram in Fig. 1.3 as the gap between the filled state μ_{N-1} and the next empty state μ_N. Fabrication methods and material type become important because as the size of the dot decreases, the gaps between each state in the Coulomb energy increase so that the E_C required exceeds the thermal energy $k_B T$ of the environment for better detection of single electrons.

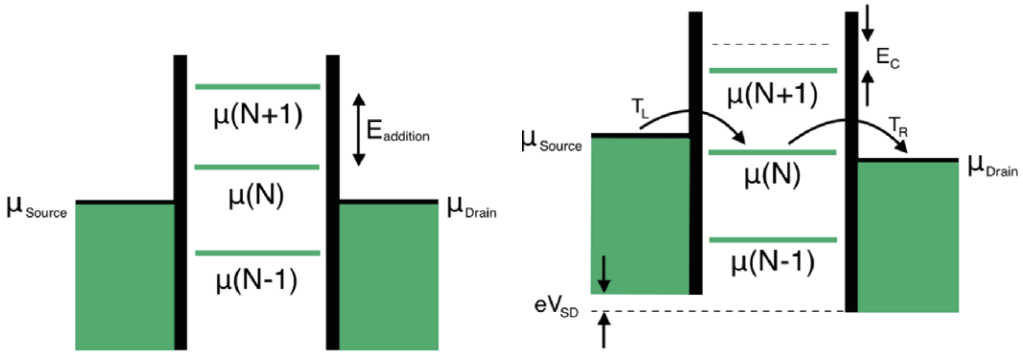

(a) (b)

Figure 1.3: The Quantum Dot is electrostatically confined between two potential barriers, denoted T_L (left barrier) and T_R (right barrier), which isolate the dot from the source and drain leads, respectively. The horizontal lines within the dot represent discrete, quantised energy levels arising from quantum confinement. The electrochemical potential $\mu(N)$ corresponds to the energy required to add the N^{th} electron to the dot. The addition energy, $E_{addition}$, is the total energy required to add one more electron (eq. 1.13). Electron transport occurs when the electrochemical potential of the dot aligns with the Fermi levels of the source (μ_s) and drain (μ_D). When no alignment occurs, Coulomb blockade prevents current flow.

$$\mu_{N+1} = \frac{e}{C_\Sigma}[(N+\frac{1}{2})e + C_g V_g] + E^K_{N+1} \tag{1.13}$$

When the electrochemical potential of the dot aligns with the source or drain, i.e. $\mu_{N+1} = \mu_{Source} = \mu_{Drain}$ in Figure 1.3, an addition of electrons to the dot becomes desirable. The electrochemical potential of the N+1 state μ_{N+1} will exceed the potentials at the source μ_{Source} and the drain μ_{Drain}, where there is no current flow or, ie, the Coulomb blockade. By tuning the gate voltage V_g (or eV_{SD}) in Figure 1.3b, the N number of electrons in the dot can be sensed by the current flow through the dot, which experimentally can be plotted by fixing V_{Source} (or V_{Drain}), and then sweeping V_g with V_{Drain} or (V_{Source}), which exhibits a characteristic known as Coulomb blockade diamonds.

1.2.2 Spin Qubits

Spin qubits utilising electrons housed in Quantum Dots (QDs) are a promising building block for quantum computing, with several implementations and materials

[18]. Quantum Dots are semiconductor nanostructures in 3D physical confinement that can scale in the range of 2-10 nm and have 100-10,000 atoms in them [3]. The spin of an electron produces a small magnetic field distinguishable from its orbital motion, and measuring this can give us information such as its angular momentum [19] [20] [21].

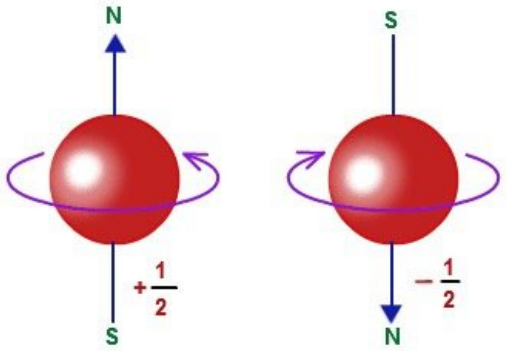

Figure 1.4: An electron spin in a Quantum Dot, spinning either up or down [3]

Unlike its alternatives, such as superconducting and Majorna qubits, Quantum Dots provide longer coherence times T_2^* and scalability. Through Electron Spin Resonance (ESR) [20], the spin of an electron encodes information in the spin-$\frac{1}{2}$ of a qubit. Then, by additional manipulation, a two-spin entanglement becomes an intriguing and plausible host for quantum computing. As a result of their nature, qubits in QD encounter difficulties with slow control and readouts [22] [2] [23].

In the functioning of qubits on a Quantum Dot, the coherence times T_2^* are crucial to executing qubit operations; hence, the time required for the control signals T_π must operate within the coherence limitations. The fabrication of Quantum Dots to attain longer coherence durations is still the subject of intensive research. In this project, we are primarily concerned with the timings of microwave pulses for rapid spin control. In these microwave experiments, it is also necessary to identify signal dependencies, such as amplitude, to investigate the relationship between SNR and the Rabi oscillation quality factor. Popular methods for determining qubit fidelity include Clifford-based randomized benchmarking and the qubit operation test. [24]

1.2.3 Charge Qubits in a DQD

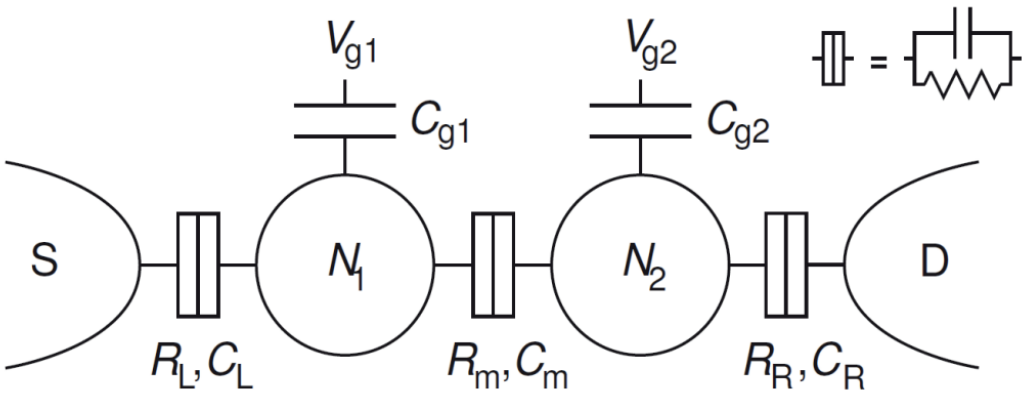

Figure 1.5: Double Quantum Dot illustrated by resistors R and capacitors C, each dot island represented by N_1 and N_2[2]

Coherent charge oscillations were first demonstrated in GaAs DQDs [25] [26]. A Double Quantum Dot is formed when two dots are coupled to each other in series through a tunnel barrier (R_m, C_m), and electrodes of a source electrode (S) and a drain electrode (D). This is better represented when treating the electrodes as a network of tunnel resistors (R) and capacitors (C) as seen in Figure 1.5. Here, a two-level system is constructed with the left and right dots represented by the eigenstates $|L\rangle$ and $|R\rangle$, respectively. Charge Qubits work on the basis of current sensing and the spatial position of an electron tunneling. By sensing the electron to exist in the left or right dot, we can logically equate the occupation in the dots to the two logical qubit states such that $|L\rangle \equiv |0\rangle$ and $|R\rangle \equiv |1\rangle$, now additionally with tunnel coupling t_c, the electron wave function being delocalized across the two dots is the mixing between two states: superposition. [2] [27] [28] [29]

1.2.4 Decoherence in Charge Qubits

Qubits hosted in semiconductors are known for their susceptibility to environmental noise, notably by the 1/f background noise at finite detuning [30]. Experiments [31] [32] [33] have quantified these effects and motivated strategies for dynamical decoupling and device material optimisation.

The interaction of a qubit with the environment, which destroys the linear superposition and collapses its quantum state, is known as decoherence. In contrast, coherence is the preservation of the quantum state during superposition. This is an

essential metric in judging the ability of the qubit host; the Quantum Dot, in this case, as an effective information carrier. T_2^* is the decay constant, known as the dephasing time, the rate at which the initial superposition state devolves back to an equal classical probabilistic mixture of the two superposition states, where the state cannot be predicted anymore.

1.3 Carbon-nanotube DQDs

Although spin qubits can be hosted on many material platforms, including GaAs and silicon, this work focuses on carbon nanotube (CNT) double Quantum Dots (DQDs). Early CNT transport experiments [34] [35] revealed one-dimensional confinement, while spin-orbit and valley coupling were established [36][37]. Subsequent demonstrations of CNT Double Quantum Dots [38] and cavity-coupled devices [39] [40] have positioned CNTs as promising hosts for electrically driven spin and charge qubits.

Double Quantum Dots can be defined along a CNT using local gates, allowing control of single electrons in distinct quantum wells. Strong spin-orbit coupling and large orbital level spacing enable coherent spin manipulation using electrical fields [36]. By coupling to microwave resonators [41] [39] and more recent cavity-embedded DQDs [40] have demonstrated fast, dispersive charge readout. In this work, we used a suspended CNT device operated in the double-dot regime at millikelvin temperatures. Control is achieved via microwave pulses, and readout is performed using radio-frequency reflectometry of the charge sensor signal.

Chapter 2

Instrumentation and Measurement Setup

This chapter outlines the instrumentation framework developed to perform precise control and readout of spin and Charge Qubits hosted in carbon nanotube Quantum Dots. The experiments required low-latency, high-resolution timing, and signal acquisition at microwave and radio frequencies. A central goal was to configure an integrated system capable of performing pulsed spectroscopy, Rabi oscillation, and Ramsey interference measurements at cryogenic temperatures.

Two commercial FPGA-based instruments from Zurich Instruments, the UHF-Quantum Analyzer (UHF-QA) and the UHF-Lock-in Amplifier (UHF-LI), were used to perform fast reflectometry readout. These devices share a common hardware platform, but differ in firmware-level processing of digital signals.

In addition, a Keysight M8195A Arbitrary Waveform Generator (AWG) was used to generate high-speed control pulses. Custom MATLAB drivers were written to automate waveform upload and synchronised triggering between instruments.

Although the instruments were commercially supplied, significant effort was put into configuring and synchronising their behavior for nanosecond-level timing control. This included programming integration windows, adjusting filter delays, and characterising device latency.

The remainder of this chapter provides a detailed technical description of each device, followed by the timing characterisation, pulse generation strategies, and

system-level integration needed to enable qubit measurements.

2.1 Zurich Instruments (UHF-QA and UHF-LI)

Two key FPGA-based instruments from Zurich Instruments, the Ultra-High-Frequency Quantum Analyzer (UHF-QA) and the Ultra-High-Frequency Lock-in Amplifier (UHF-LI), were employed to generate RF signals and process reflected signals in qubit measurement experiments. Although both instruments share identical hardware features, such as input/output ports, 1.8 GSa/s analog-to-digital converters (ADCs), trigger ports, and FPGA back-end, their internal signal processing methods differ significantly. The UHF-QA operates primarily in an integration-based measurement mode tailored for fast, time-gated experiments, while the UHF-LI applies continuous dual-phase digital lock-in demodulation suited for frequency-domain characterisation. Each instrument thus served a complementary role within the measurement pipeline: initial device characterisation using the UHF-LI, and high-speed pulsed measurements with the UHF-QA.

Both instruments feature a cross-trigger engine hardware module which is crucial for real-time exchange of signals between the UHF's Arbitrary Waveform Generator and the qubit measurement module by the use of triggers, marker, and register signals.

2.1.1 UHF-QA (Integration Mode)

The UHF-QA is specifically designed for quantum computing measurements, providing rapid time-domain integration of RF signals reflected from qubits. The input signals are digitised at a rate of 1.8 GSa/s with an effective measurement bandwidth of 600 MHz. These signals pass through an internal Digital Signal Processing (DSP) pipeline featuring ten parallel integrator channels, each capable of applying user-programmed integration weights over a window of up to 4096 samples ($2.3\mu s$ duration). The integrated results provide direct information on the qubit state, allowing real-time decision making and low-latency digital feedback via the instrument's DIO ports. Such capabilities are critical for executing precise and time-sensitive experiments, including Rabi and Ramsey pulse sequences, where accurate timing

and state discrimination are paramount. [5]

2.1.2 UHF-LI (Lock-In Demodulation)

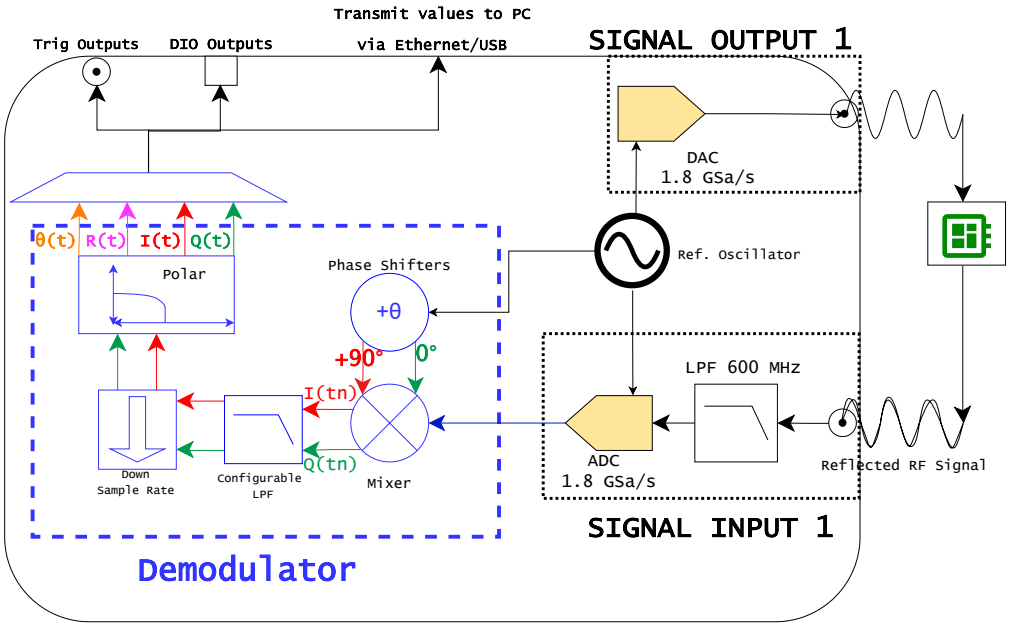

Figure 2.1: Functional block diagram of the Ultra High-Frequency Lock-in Amplifier, highlighted in blue box: Demodulators & Oscillators, shows the lock-in demodulation signal pathway. [4]

The UHF-LI differs from the UHF-QA primarily in its digital lock-in demodulation approach, employing dual-phase homodyne detection to measure continuous amplitude and phase relative to an internal reference oscillator. Following digitisation at $1.8 GSa/s$, the incoming signal undergoes digital mixing and passes through a configurable low-pass filter. Filter order and time constant (τ) define a trade-off between bandwidth and measurement latency, directly affecting the instrument's response speed and noise suppression capabilities. With an input dynamic reserve of $-118 \frac{dBc}{Hz}$ and noise floor of $4 \frac{nV}{\sqrt{\text{Hz}}}$, the UHF-LI is optimally suited for sensitive, noise-critical characterisation tasks, such as initial reflectometry measurements of Quantum Dot devices prior to integration of cryogenic amplifiers like the Josephson Parametric Amplifier (JPA). [4]

Although both instruments share similar hardware - including RF I/O ports, ADCs, DACs, and signal bandwidth up to $600 MHz$ — the UHF-LI is optimized

for continuous signal demodulation [4]. During the early phase of this project, the UHF-LI was used to probe a shorted carbon nanotube device forming part of a forthcoming publication.

2.1.3 Lock-in demodulation and filter tuning

A key configurable component is the digital low-pass filter applied prior to demodulation. This filter, implemented as an exponentially weighted moving average, exhibits characteristics similar to those of a continuous-time RC filter. The filter is characterised by its order n and time constant τ: higher-order filters provide stronger high-frequency attenuation, but introduce greater group delay. This trade-off between bandwidth and response time must be carefully managed, especially in timing-sensitive pulse experiments. The filter transfer function is given by:

$$H_n(\omega) = \left(\frac{1}{1+i\omega\tau}\right)^n \tag{2.1}$$

In pulsed experiments, this group delay can shift the apparent arrival time of signals, potentially misaligning the timing of integration windows or introducing errors in cross-instrument synchronisation. To balance the signal-to-noise ratio and latency, a second-order filter with $\tau = 0.1$ μs was typically used throughout the reflectometry experiments described later.

2.1.4 Comparison between UHF-QA and UHF-LI

Both pieces of equipment have the same hardware and the FPGA used, but the defining feature is how the incoming digitised signal is processed after the ADC. There is less user flexibility for the lock-in, since we only change which line the reference signal sources, the demodulator, the demodulation sampling rate, and the low-pass filter applied. For the UHF-QA, instead of the schematic demodulator seen in Figure 2.1, the FPGA is reprogrammed to replace it with the integrator of Figure 3.4.

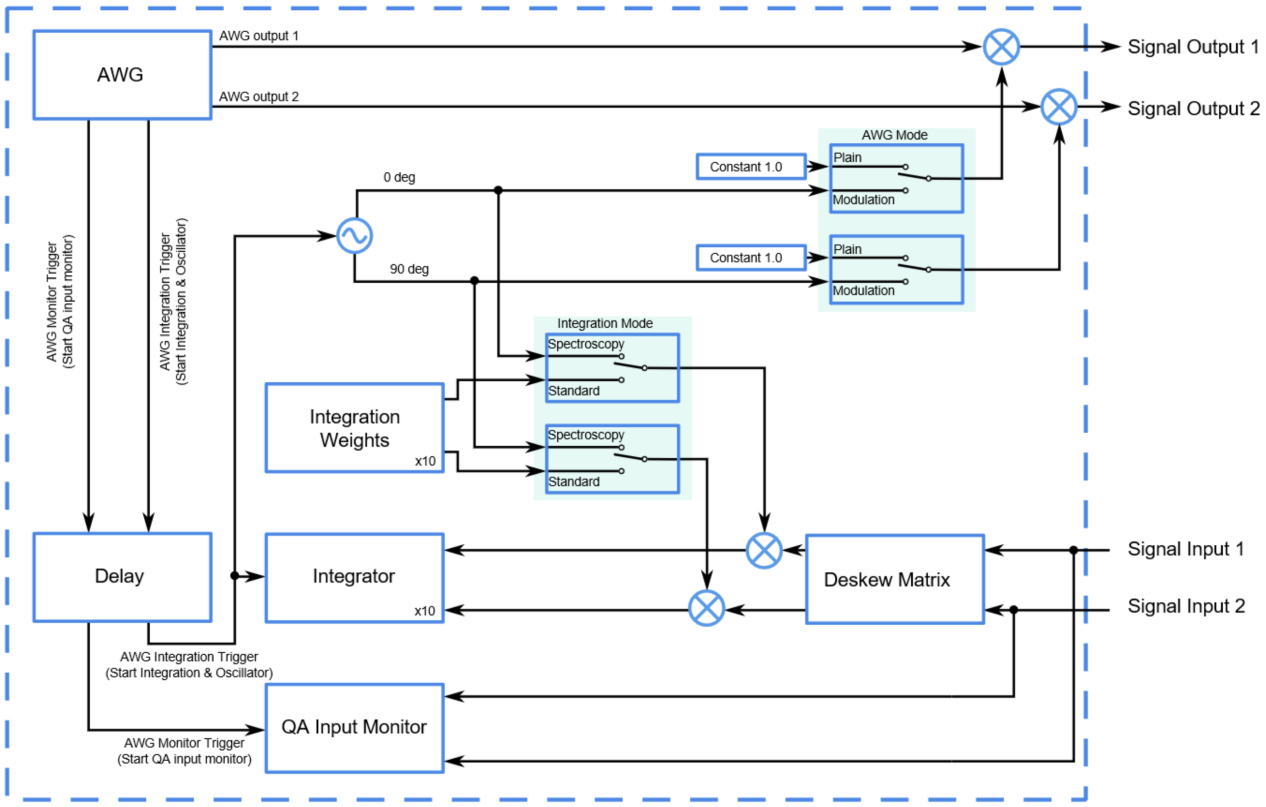

Figure 2.2: Block diagram of the UHF-QA Qubit Measurement Unit with ten parallel integrator channels. Each channel has a user-programmable integrator signal. In spectroscopy mode, the integrators use a digital oscillator as the reference source—mimicking the demodulation process used in the UHF-LI—for high-precision frequency-resolved measurements. [5]

The integration weights in UHF-QA are user-programmable and span a total duration of 2.3μ s, corresponding to an effective sample rate of approximately 1.781 GSa/s. In contrast, the UHF-LI demodulator operates at a significantly lower maximum sampling rate of 1.6 MSa/s. However, this higher speed capability of the QA comes with the constraint that integration is limited to a fixed window of 4096 samples. In spectroscopy mode, the QA uses an internal digital oscillator as its reference signal, functioning similarly to the UHF-LI. Although the UHF-LI offers broader software-level configurability for general-purpose measurements, the UHF-QA is tailored for quantum computing applications, providing built-in hardware features such as deskew matrices, I/Q plane rotation, cross-talk suppression, state thresholding, and fast digital feedback via high-speed DIO output.

Overall, although both instruments were commercially provided, configuring

and comparing their signal processing modes was an essential part of my experimental work, particularly in selecting the optimal read-out path for low-latency integration in CNT-based qubit control.

2.1.5 Summary

Feature	UHF-QA	UHF-LI
Signal Processing Mode	Time-domain integration using a user-defined weight function	Dual-phase digital lock-in detection
Signal processing Mode	Integration over programmable windows (e.g. 2.3µs using 4096 samples)	Output sampled at up to 1.6MSa/s post-demodulation
Filter/Weighting	FIR-like weighting via user-defined vectors	IIR low-pass filter with user-settable order and time constant (30ns to 76s)
Optimised For	Qubit readout with nanosecond-level timing, fast feedback, and digital output (DIO)	General-purpose amplitude and phase demodulation across wide bandwidths
Used For	Pulsed reflectometry in Rabi and Ramsey measurements	Initial CNT device characterisation and tank circuit testing
Output Data Format	Integrated IQ results with optional state thresholding and histogramming	Demodulated time-domain amplitude and phase traces
Latency Considerations	Determined by integration window length (e.g. 2.3µs max)	Determined by filter order and time constant (group delay)

Table 2.1: Comparison of UHF-QA and UHF-LI functionality and configuration in the measurement setup. Both devices use a shared 1.8 GSa/s ADC front-end but differ significantly in signal processing, latency, and user interaction.

To clarify the different roles of UHF-QA and UHF-LI in this measurement setup, Table 2.1 summarizes their key features and configurations. Although both devices share identical front-end hardware, their FPGA signal processing modes differ substantially.

2.2 Keysight M8195A Arbitrary Waveform Generator

In this project, the Keysight M8195A Arbitrary Waveform Generator (AWG) served as the primary instrument to generate high-speed microwave control pulses that drive qubit transitions. Operating at sampling rates up to 65 GSa/s with 15 ps timing resolution, it enabled coherent manipulation of Charge Qubits in double Quantum

Dot devices. These sequences typically consist of Gaussian or square pulses tuned for specific quantum operations (e.g., $\frac{\pi}{2}$ or π rotations)

By uploading waveform sequences to its internal FPGA memory and configuring trigger synchronization with Zurich Instruments hardware, precise pulse-timing control and feedback-based qubit experiments (such as Rabi and Ramsey) were realized.

The AWG generates microwave pulses via its DACs from samples stored in memory. These pulses are then sent to the gate electrodes of the qubit for coherent control.

2.2.1 In-house designed M8195A software driver

The workflow, shown in Figure 2.3, begins with defining the waveform parameters in MATLAB, which are converted into sampled arrays with associated digital markers. These are segmented and validated before being encoded into SCPI commands and sent to the AWG. This setup allowed for automated experiments such as Rabi and Ramsey measurements, and serves as a foundation for the feedback sequences discussed in Section 2.2.4 onward.

The Keysight M8195A AWG includes a GUI-based software panel to generate and sequence standard waveforms. However, it lacks the flexibility required for automating pulse sequences in Quantum Dots experiments. To address this, I developed a custom MATLAB-based driver that automates waveform generation, segmentation, marker assignment, and SCPI command handling over TCP/IP. Figure 2.3 illustrates the core workflow of the MATLAB driver, showing how high-level pulse definitions are translated into waveform segments, encoded as SCPI commands, and uploaded to the AWG for precise nanosecond playback. This sequence enables time-critical qubit control in the experiments described later in this chapter.

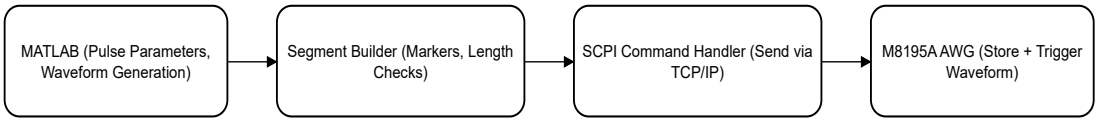

Figure 2.3: Workflow of the custom MATLAB driver developed for the Keysight M8195A AWG. The diagram shows how user-defined pulse parameters are converted into waveform segments with markers, formatted into SCPI commands, and uploaded via TCP/IP for precise playback. This software bridge enabled fast, automated qubit control in later experiments and integrated the AWG into the wider measurement framework used throughout this thesis.

2.2.2 Internal Signal Processing Path

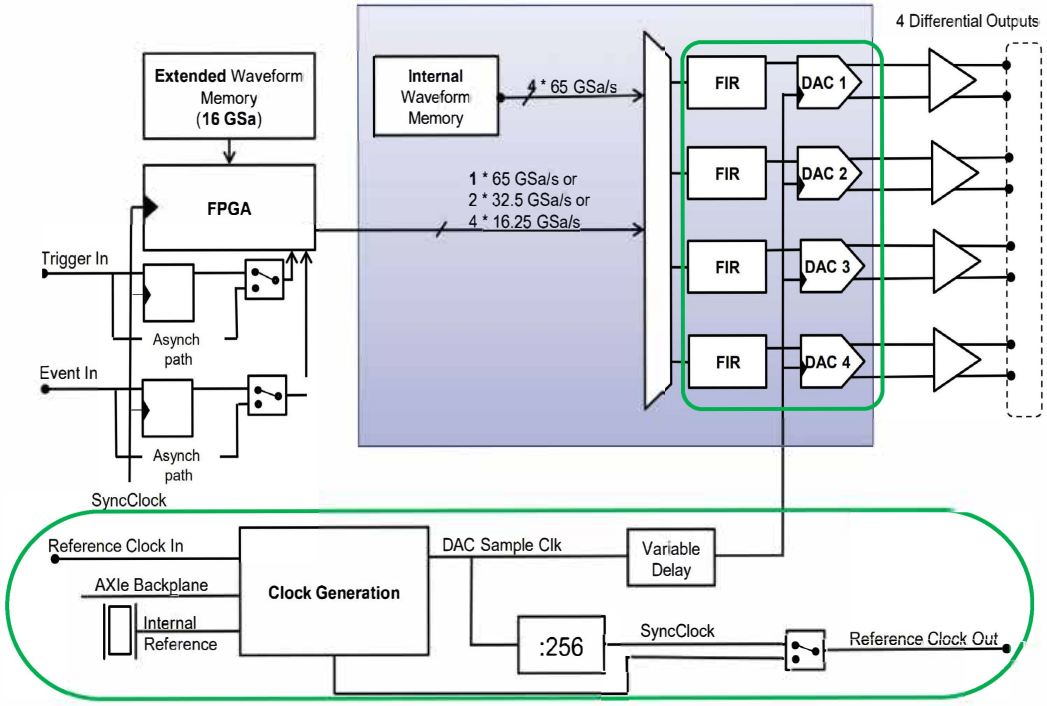

Figure 2.4: Simplified architecture of the M8195A AWG signal path, highlighting its key components in green: high-speed DACs, FIR interpolation filters, and internal clock management. These hardware blocks shape the spectral fidelity and timing accuracy of generated waveforms, and contribute to signal artefacts such as latency, bandwidth roll-off, and rise-time distortion discussed in later sections.

Module name	Description and functions
M8195A.m	A superclass handler which Module.m subclass inherits. Initialises an instance for each module part of the driver and attempts connection with the M8195A through TCP/IP interface.
Module.m	The subclass of M8195A.m has the most useful high-level functions, such as querying for node values, module initialisation, and writing to FPGA memory.
OutputModule.m	Everything related to the signal outputs, e.g., turning the output on or off, setting amplitude value, channel memory source, time delay, differential offset, channel divider (1, 2 or 4), output FIR filter amplitude.
SequencerModule.m	Manages sequences to be uploaded to the memory with many logic and rules to ensure the segments to be uploaded is suitable to be played out without throwing errors in the hardware
TriggerModule.m	Manages everything related to triggering, such as setting the trigger mode, armed mode, source of the trigger, events, and force trigger events to occur
ClockModule.m	Manages the DAC sampling frequency, reference clock, adjust for clock cable delay
SDWaveformModule.m	Manages memory of the FPGA and uploads MATLAB-defined waveforms, synthesising some common signals (sinusoidal, Gauss, etc.) quickly to the AWG to be played.

Table 2.2: M8195A Matlab driver modules

While waveform construction and upload are handled by the MATLAB driver, the spectral fidelity and output quality of signals are ultimately shaped by the internal architecture of the M8195A AWG. Figure 2.4 shows a simplified block diagram of the internal signal processing architecture of the M8195A AWG, including its high-speed DACs, digital interpolation filters, and clock generation. In particular, the finite impulse response (FIR) filters play a critical role in bandwidth shaping and suppression of spectral replicas, directly affecting how faithfully an arbitrary waveform is synthesised. These hardware elements impose non-idealities and delays that must be considered when aligning pulse sequences and assessing experimental signal quality.

2.2.3 Waveform Upload Sequence

Once the MATLAB driver has generated waveform data, it must be validated, segmented, and uploaded to the M8195A AWG in a format compatible with hardware playback. This process involves ensuring correct waveform structure, normalising amplitude ranges, assigning digital marker signals, and enforcing compliance with AWG's memory alignment and granularity requirements. The goal is to ensure that the waveform is correctly interpreted by the AWG, is seamlessly triggered during the experiment, and is properly aligned with other instruments such as the UHF-QA.

The waveform is first checked to ensure that it is a column vector; if not, it is transposed accordingly. Then the amplifier scaling is applied so that the maximum absolute value fits within the $\pm 1V$ output range of the DAC. A corresponding digital marker signal is generated, typically a square pulse, which defines the active region of the waveform to trigger other instruments such as the UHF-QA.

To comply with the hardware constraints of the AWG, the waveform length is padded to satisfy the granularity rules; for example, the number of samples must be a multiple of 256 divided by the selected sample rate divider. Segment lengths must also fall within the supported memory range (minimum 1280 samples, maximum 2^{23}) [8]. Once validated, the waveform data is arranged in a four-row memory matrix corresponding to the four AWG DAC output channels. Even if only one or two channels are used, all four must receive valid memory data. Unused channels are padded with zeros to maintain alignment and satisfy the AWG upload model. This enforced structure guarantees consistent memory layout and playback logic across all outputs.

The waveform and marker data are then uploaded in this structured format over TCP/IP using SCPI commands, and the AWG is armed for trigger-based playback.

Beyond simply uploading waveforms, the use of the M8195A in this work was shaped by the need to generate nanosecond-scale microwave pulses suitable for spin-qubit manipulation. Unlike conventional AWG applications that produce continuous waveforms or carriers modulated with IQ, this system relied on the direct digital synthesis (DDS) capabilities of the M8195A to produce isolated time-gated

RF bursts up to $20GHz$. This approach eliminated the need for analog upconversion and mixers, thereby reducing potential phase instability. Achieving pulse widths as short as $150ps$ required careful balancing of sample rate, memory constraints, and granularity compliance, as well as tight control over marker alignment for external triggering. These constraints demanded a waveform generation strategy tightly coupled to the upload and playback logic described above.

2.2.4 Trigger feedback experiment

The two trigger operations in the M8195A are synchronous and asynchronous modes. The internal clock, which is used as a reference for all samples for signal generation, is known as the Synch clock, and it adjusts itself every time the DAC sample rate is changed from the software side.

$$\text{Synch Clock} = \frac{\text{DAC Sample Rate}}{256} \tag{2.2}$$

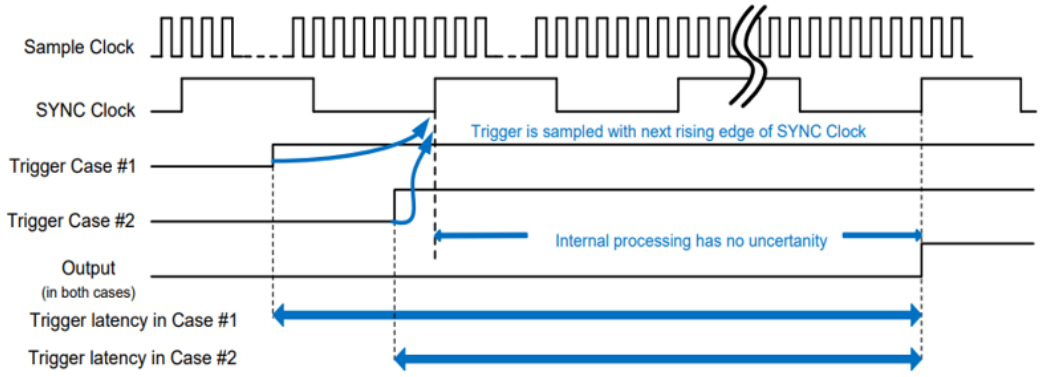

Figure 33: TRIGGER/EVENT synchronous to the sync clock (synchronous tmode)

Figure 2.5: Synchronous mode operation sends an active trigger where the output sample always depends on the SYNC clock instead of the sample clock in asynchronous mode. The sample clock is the internal reference of the device for all samples to signal generation. The Synch clock adjusts itself every time the DAC sample rate is changed from the software side. This delay will always ensure a constant latency of 157 synch clock cycles from when a trigger event is detected in synchronous mode, and the DAC sample rate range is 53.76 GSa/s to 65 GSa/s user manual [6]

In synchronous operation mode, for consistency, the internal sample clock of the M8195A is also expected to be shared with the UHF devices. This reference

clock synchronises the incoming trigger signal with the output and the UHF instrument, generating and processing signals using the same reference signal. Wire lengths mainly dominate the phase delay for this master clock, but this is constant, does not have much noise variation, and is characterised. This is preferable for fast experiments with multiple instruments connected in a network with timing constraints. It ensures that we can reliably expect how long the internal hardware will take to send a signal out and that only time latency outside the M8195A will be taken into account. Alternatively, the asynchronous mode will introduce an uncertainty of 40,192 clock cycles $\equiv \pm 100$ ps, which is 618.34 ns ± 100 ps if operating at 65 GSa/s. [6]

These operational modes impose different timing behaviors, which makes it essential to experimentally quantify the trigger-to-output latency, as described in the following section.

2.2.5 Finding the initialisation time latency

Precise timing alignment between instruments is critical in pulse-based quantum experiments. To ensure that the M8195A AWG could be reliably triggered by the UHF device and output a pulse with consistent timing, we experimentally characterised its trigger-to-output latency.

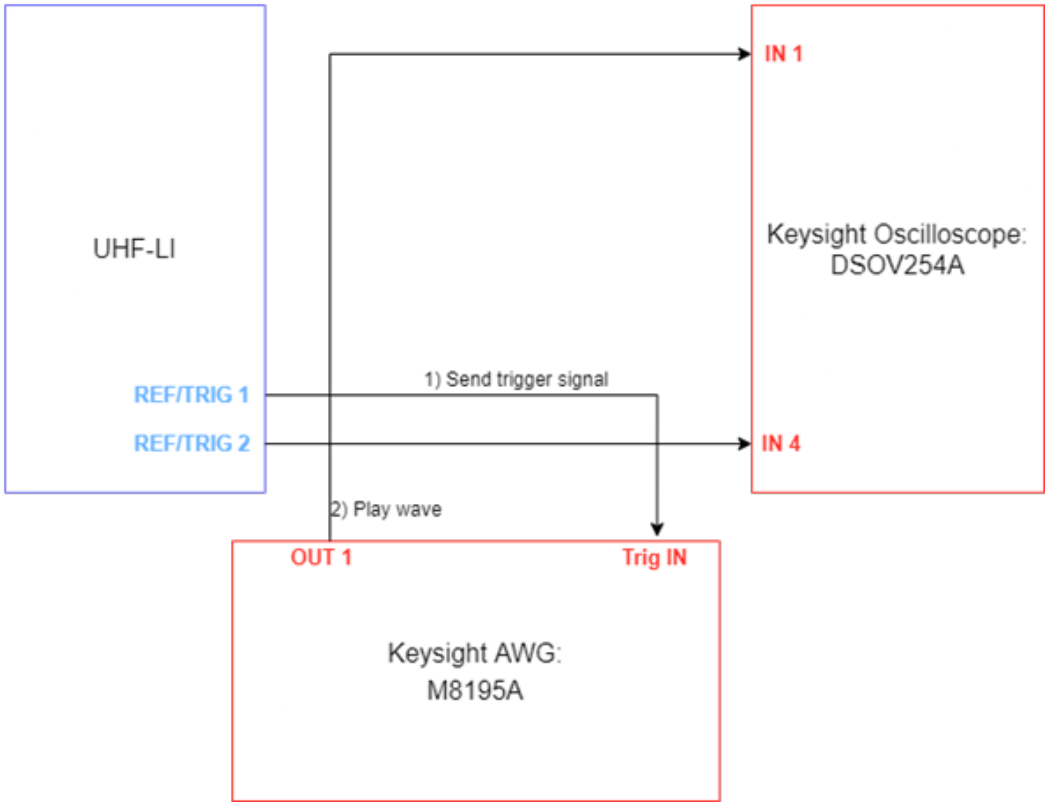

Figure 2.6: Schematic of the experimental setup used to measure the trigger-to-output latency of the M8195A AWG. A digital trigger signal is generated by the UHF instrument and received by the AWG. The AWG responds with a square waveform, and both signals are captured by a high-bandwidth oscilloscope for latency measurement via edge timing comparison.

As shown in Figure 2.6, the UHF instrument generated a digital trigger pulse to initiate the playback of the waveform on the AWG. The resulting output, a square wave with 50% duty cycle, was captured by a Keysight DSOV254A high-bandwidth oscilloscope. By averaging over 1,024 acquisitions and applying threshold-based edge detection, the time delay between the incoming trigger and the AWG output was measured.

The measured latency was found to be 626.26 ns, a value that was used in later sections to align integration windows and compensate for signal path delays in the overall timing architecture.

2.2.6 Integration trigger feedback signal

To coordinate readout timing during pulsed qubit experiments, the M8195A AWG must send a digital marker signal to trigger the UHF-QA's integration window. This was implemented using the AWG marker output: a high digital signal is aligned to the second of two square waveform segments played by the AWG. These two pulses emulate a Ramsey-like structure, where the second pulse is immediately followed by the UHF-QA integration window.

The UHF-QA was configured to begin integration after detecting the falling edge of the AWG marker. Using the QA's monitor module, the delay between this trigger and the first captured sample was measured as 33.69 ns. This delay is attributed to physical cable propagation, internal routing delays, and trigger threshold detection time. Although not a full Ramsey sequence, this timing test served to calibrate the feedback timing accuracy of the AWG-QA integration pipeline.

2.2.7 Rise and fall time uncertainties

The AWG is operated at the highest resolution possible at 15.38 ps and $\frac{\pi}{2}$ pulses are captured by the oscilloscope to characterise and investigate the expected vs. observed rise and fall times.

Coded rise time $/ps$	**Measured rise time** $/ps$	**Coded fall time** $/ps$	**Measured fall time** $/ps$
15.38	35.41	15.38	43.98
30.76	44.88	30.76	47.29
46.15	52.71	46.15	41.24
61.52	59.55	61.52	57.12
76.92	82.20	76.92	58.85
92.32	90.93	92.31	71.92
107.69	99.80	107.69	85.25
123.08	108.12	123.08	93.68

Table 2.3: M8195A the coded rise & fall times vs. the actual captured rise & fall times observed

2.2.8 Real-world pulse distortion

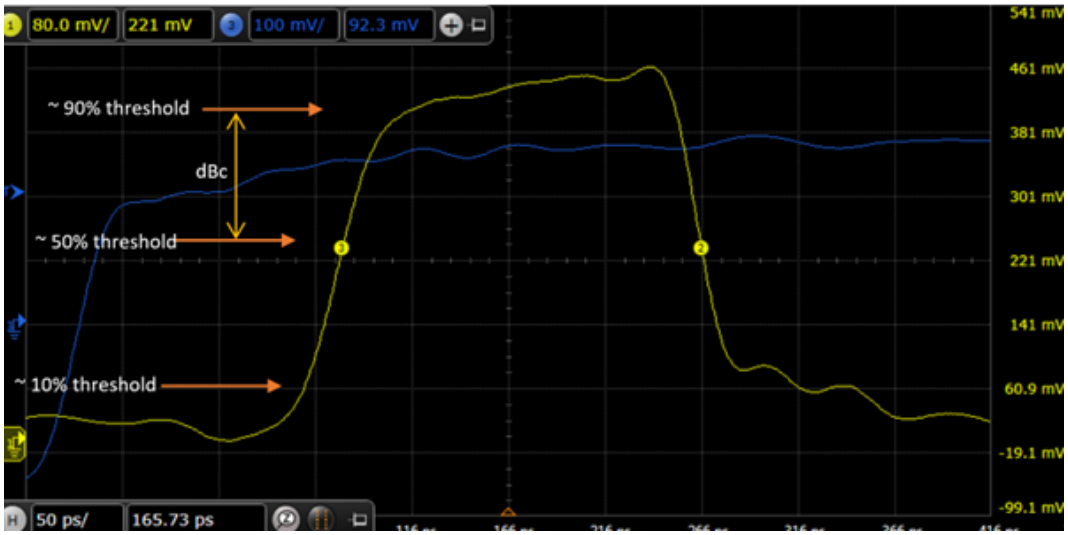

Figure 2.7: Zoomed-in capture obtained with a 25 GHz oscilloscope connected to the M8195A AWG (yellow trace) and the UHF output (blue trace), showing the second pulse from Table 2.3. The annotated markers indicate the threshold levels used for timing calibration. When the UHF signal (blue) is high ($\tilde{1}$90 mV), the corresponding M8195A pulse is detected after approximately 100 ps, with its 90 % threshold reached about 140 ps later. Timing measurements are defined by locating the four cardinal points of the pulse waveform (10 %, 50 %, 90 % thresholds and the baseline reference). As discussed earlier, the choice of output and demodulation filters influences the precision of these timing extractions [7] [8]. The use of 10 %, 50 %, 90 % threshold levels accounts for overshoot and DAC-synthesiser filtering inherent to the M8195A AWG.

There can be several contributing factors to the distortions that can affect the captured signal from the programming point of view. The reconfigurable output digital filters cause overshooting due to the higher sidebands (higher rate of rise) present in the rise time, which are filtered and add overshoot [8].

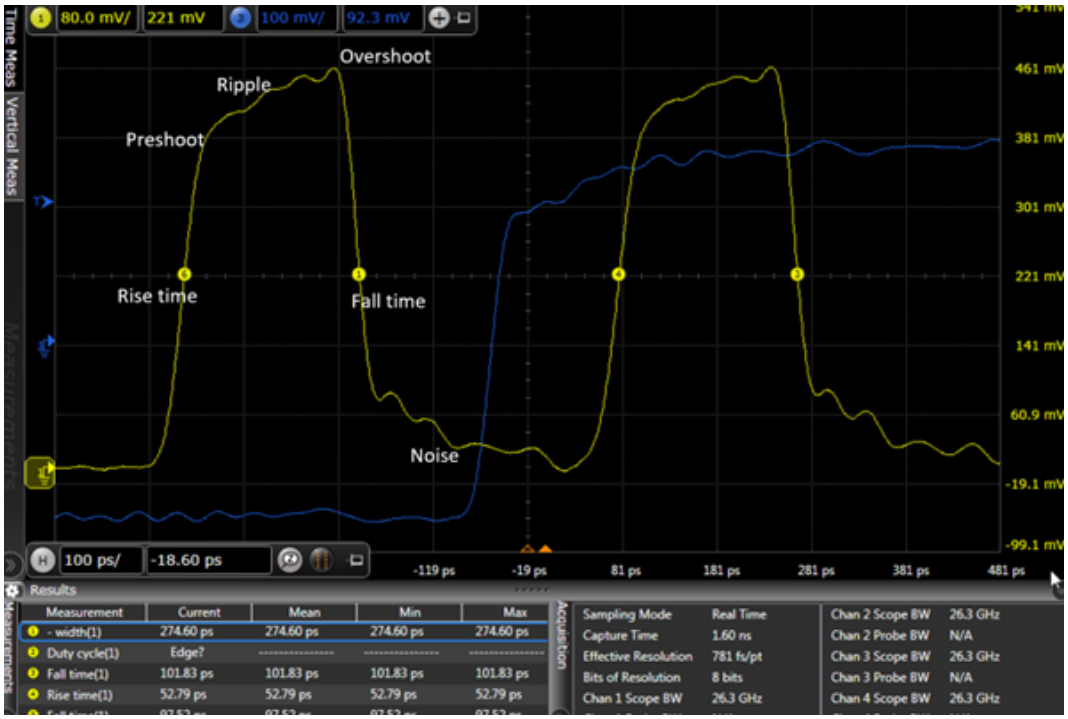

Figure 2.8: Pulsed measurement capture similar to Figure 2.7, except here the blue trace represents a marker output from the M8195A AWG that transitions high precisely when the second pulse is generated. In practice, this marker output is connected to a trigger input on the UHF instrument to indicate the onset of the second pulse, allowing a programmable delay to define the start of readout. In this example, the horizontal time axis shows the marker signal rising at approximately $\tilde{1}9$ ps, while the second pulse (yellow) returns to ground at about 281 ps, corresponding to a total delay of 300 ps between trigger onset and pulse termination. This delay value sets the timing offset for initiating integration or demodulation in the UHF system. Real-world waveform distortions observed in the first pulse (yellow) are annotated for reference.

The measurements from Figures 2.8 and fig:realworlddistort1 were taken using a 25 GHz oscilloscope Keysight DSOV254A.

2.3 Overview of Cryogenic Setup and RF path

This section describes the dilution refrigerator and wiring setup used for probing hte Quantum Dot sample

This section describes the dilution refrigerator and wiring setup used for probing the Quantum Dot sample as best seen in B. The setup mainly consists of three wiring lines which are highlighted by coloured dashed lines: JPA and readout lines in red, DC lines blue, Microwave lines in purple. The construction and setup of the

components and fridge setup was designed and setup by other members in the Quantum Devices group.

Within each temperature stage, copper-copper cables (UT-085c) are used. Between temperatures the rest are stainless steel-stainless steel (UT-085-ss-ss). The Microwave lines from 300-4K are Beryllium copper-stainless steel (UT-085B-SS). All semi-rigid coax connection provide very low losses from -70 dB/100ft up to -400 dB/100ft at 10 GHz.

2.3.1 RF amplification and Josephson Parametric Amplifier (JPA)

A detailed theoretical understanding of the JPA is beyond the scope of this thesis; further details are available in VTT research publications [42], therefore it will briefly be mentioned as part of the RF readout signal chain. The JPA is integrated into the RF signal chain to provide near quantum-limited amplification of the reflected readout tone from the resonant circuit coupled to the quantum dot. It operates in the frequency range of 500–900 MHz with a typical gain of +40dB and a bandwidth of approximately 20–40 MHz, depending on pump power and bias conditions. The amplifier contributes a negligible effective noise temperature, typically below 0.1K, thereby substantially improving the signal-to-noise ratio (SNR) compared to conventional cryogenic amplifiers. The understanding of JPA is out of scope for this project and can be read more online published by VTT Research Finland [42].

The JPA is mounted at the 10–20 mK stage (mixing chamber) and is followed by a cryogenic low-noise amplifier (LNA, model LNF-LNC0.2_03A) positioned at the 3.5 K stage. The LNA provides an additional +45 dB of gain with a noise temperature of approximately 4K over the same operating frequency range (500–900 MHz). This amplification chain ensures that the weak reflected signal from the quantum dot resonator is sufficiently amplified before transmission to room-temperature electronics for demodulation.

To ensure proper isolation between the JPA and the sample, a series of cryogenic circulators and isolators are installed near the mixing chamber. These components direct the probe tone towards the sample and guide the reflected signal back to

the amplification chain while preventing back-propagation of amplifier noise and pump leakage into the quantum device. The RF lines are further equipped with attenuators distributed across temperature stages to thermalise and filter incoming signals, thereby reducing Johnson–Nyquist noise.

2.3.2 Reflectometry Tank Circuit

The reflectometry readout of the Quantum Dot device is achieved through an impedance-matching tank circuit connected to the source and drain electrodes of the sample. The tank circuit comprises a parallel network of inductors and capacitors that collectively form an LC resonator. The effective resonance frequency is determined by the total inductance and capacitance and practically, is designed such that the resonance occurs near 500 MHz, within the optimal bandwidth of the JPA and cryogenic LNA. The reflected signal carries information about the device such as charge tunnelling or movement between dots modifies the quantum capacitance of the DQD, thereby phase shifting, which is detected by demodulation electronics (UHF-QA/UHF-LI) to identify electron transitions with high sensitivity. These phase shift sensitivity of capacitance is mathematically described in equations 4.3 and 4.4.

2.3.3 DC Wiring and Filtering

The DC lines are used to provide gate and bias voltages to the quantum dot device. Each DC line passes through multiple filtering stages to suppress thermal and electromagnetic noise coupling into the device. At the 3.5K stage, each line is equipped with a copper-powder filter to attenuate broadband high-frequency noise. Following this, an RLC filter network is installed to provide strong attenuation of frequencies above 10 kHz while maintaining DC connectivity.

The RLC filter consists of a cascade of RC and LC sections, with carefully chosen component values to achieve a roll-off frequency of approximately 10 kHz. This allows low-frequency gate modulation while suppressing residual high-frequency components that could otherwise contribute to qubit dephasing or charge instability. All DC lines are thermally anchored at each temperature stage using copper posts to minimise heat load and to ensure proper thermalisation to the mixing

chamber base temperature.

2.4 Device Fabrication

The carbon nanotube devices studied in this work originate from a series of free-standing Double Quantum Dots developed within the Quantum Devices Group at the London Centre for Nanotechnology. Although I was not directly involved in their fabrication, these devices form the foundation of all subsequent measurements presented here. Their design reflects the group's broader effort to create carbon-based quantum dots with exceptionally low charge noise—an approach that directly enables the high-fidelity readout experiments described later in this thesis.

In brief, the devices consist of single-wall carbon nanotubes suspended across local gate electrodes, forming a double quantum dot that is electrostatically defined and isolated from the substrate to minimise charge noise and surface contamination.

All fabrication and design work was carried out by colleagues in the Quantum Devices Group and is described in detail in a forthcoming manuscript, "Radio-frequency readout of ultra-low-noise carbon nanotube quantum dot devices" (Ravichandar *et al.*, unpublished, submitted to Nature Electronics). My own contribution begins with the cryogenic integration, radio-frequency measurement design, and analysis of the device behaviour discussed in the following sections.

2.5 Summary of Instrumentation and Measurement Setup

- Integrated room-temperature readout and signal generation instruments which is connected to the low-noise cryogenic measurement chain for carbon nanotube DQDs based on RF reflectometry in the 0.5–0.9 GHz band (tank circuit at the device; demodulation with UHF-LI/UHF-QA).

- Investigated filtering of UHF-LI and the integrator of UHF-QA, and compared the advantages and disadvantages; suitability for types of measurements; trade-offs between configurable filter integration times vs. frequency bandwidth.

- Calibrated end-to-end timing and latencies (trigger-to-out of the AWG; QA integration delay; lock-in group delay) and aligned pulse and integration windows accordingly.

- Verified the full chain with loopback/bench tests to characterise bandwidth, gain, noise floor, and demodulation fidelity before connecting to the device.

- Explain the cryogenic and dilution refrigerator setup used in measurements and already present in laboratory, and how they interface with room-temperature equipment such as UHF-QA/LI and M8195A.

- Referenced a forthcoming publication, ”Radio-frequency readout of ultra-low noise carbon nanotube quantum dot devices” which will include more information on fabrication of sample device used.

2.6 Discussion and Results

This chapter establishes the experimental backbone for everything that follows: a reflectometry platform with sufficient sensitivity and timing precision to resolve single-electron charge motion on sub-microsecond timescales. The JPA-based readout reduces the required integration time by roughly an order of magnitude at fixed SNR, which is discussed practically further in the next chapter with measurements. The latency calibration test ensures that drive and readout are phase-coherent at the device, so that time-domain experiments are interpreted quantitatively with latency and jitter times considered.

Two practical lessons emerged. First, the M8195A pulse sequencing has to be correctly optimised by uploading samples to be played along with a synchronous clock distributed with the UHF instrument. Secondly, the filtering of readout instrument is a trade-off between noise rejection and signal latency; explicitly accounting for group delay in the integration window prevents readout amplitude smearing and underestimation. These constraints set realistic operating envelopes for the device measurements in Chapter 3 and pulsed control sequence in Chapter 4.

Chapter 3

Charge State Measurements of a Carbon Nanotube Device

RF reflectometry is very advantageous compared to other read-out methods because of the speed and non-invasive probing of the Quantum Dot. For experiments which involve qubit operations, the achievable signal-to-noise (SNR) of the experimental setup at room temperature down to the dot becomes an important factor and a requirement to be below the qubit relaxation and coherence times. Early experiments and analysis were performed to find the capacitance sensitivity of the dot and readout integration times, which also helped to optimize the signal strength and readout procedure in the future. To clarify, all the measurements included in this chapter were performed at the laboratory on a sample fitted to the dilution refrigerator.

3.1 Signal-to-Noise and charge state readout sensitivity

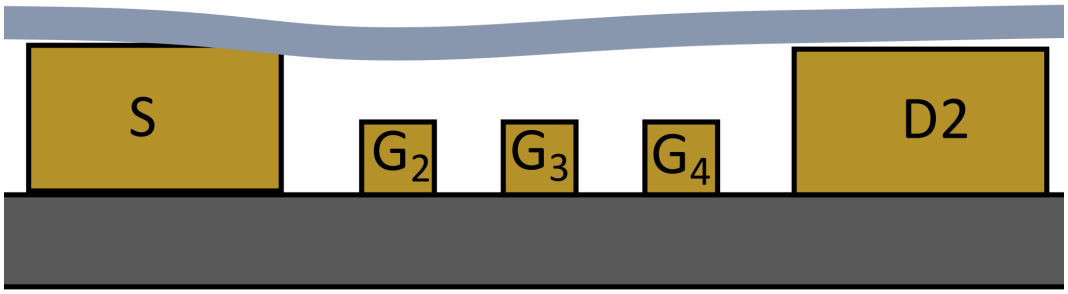

Figure 3.1: 2-D view of DQD sample with the left dot (state $|0\rangle$) represented by G_2 and right dot (state $|1\rangle$) by G_4

Two electrodes are voltage-swept at a single-electron Quantum Dot transition area. By varying the integration times of the UHF-LI demodulator and by plotting 2-D stability diagram measurements as a function of both gate voltages, we find the effect of the JPA on SNR to be an improvement of up to tenfold. The reflected amplitude is demodulated with the UHF-LI. Three different integration times were chosen at $\tau = 10\mu$s, 1μs, 0.1 μs; the results can be seen in figure 3.3.

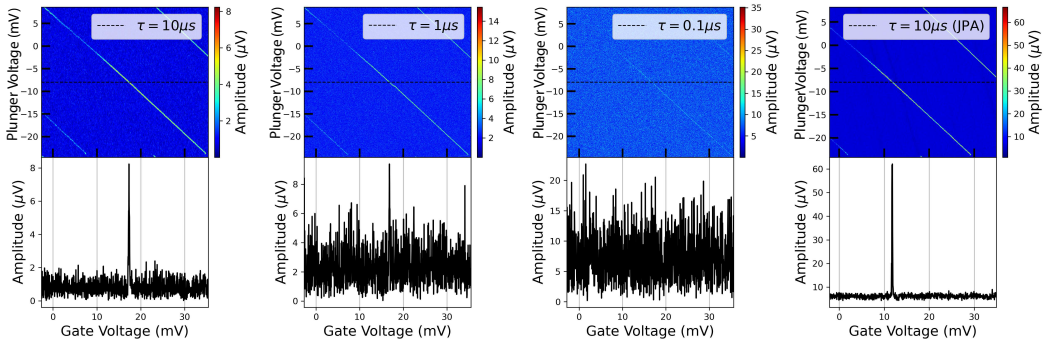

Figure 3.2: Stability diagrams taken as a function of the gate voltages and different integration times, additionally one with the JPA enabled, showing an improvement in SNR by up to an order of magnitude. Going from left to right: 1) High integration time 10μs, JPA disabled 2) Mid integration time 1μs, JPA disabled 3) Low integration time 0.1μs, JPA disabled 4) High integration time, JPA enabled.

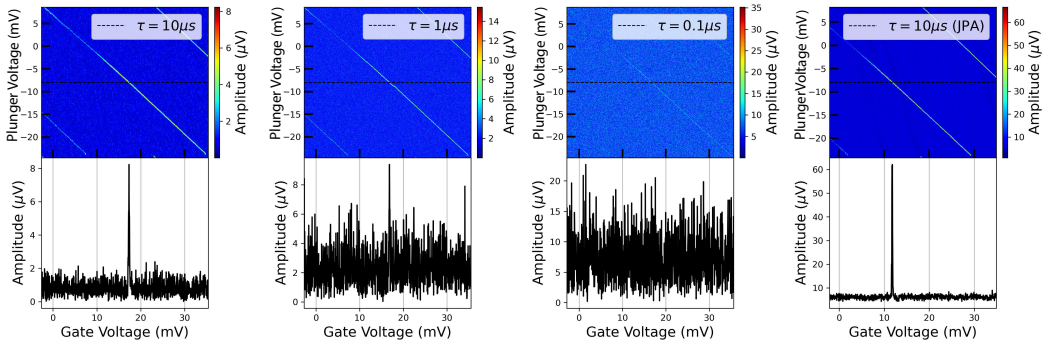

Figure 3.3: Charge stability diagrams measured as a function of gate voltages and integration time, including a comparison with the JPA enabled. From left to right: (1) high integration time (10 μS), JPA disabled; (2) medium integration time (1 μS), JPA disabled; (3) low integration time (0.1 μS), JPA disabled; and (4) high integration time (10 μS), JPA enabled. The use of the JPA results in an improvement in SNR by approximately an order of magnitude for equivalent integration conditions.

Figure 3.3 presents charge stability diagrams obtained by sweeping two gate voltages, with corresponding Coulomb peak line traces shown below each panel. In the first three diagrams (from left to right), only the integration time is varied while the JPA remains disabled. As the integration time decreases from 10 μS to 0.1 μS, the amplitude of the Coulomb peak—initially reaching up to 8 μV—becomes increasingly obscured by noise, and the surrounding noise floor exhibits greater fluctuations, leading to a visibly reduced signal-to-noise ratio (SNR). In contrast, the rightmost diagram, recorded with the JPA enabled at the same 10 μS integration time, shows a well-defined peak reaching approximately 60 μV and a markedly lower noise floor. This demonstrates that, for identical integration conditions, activating the JPA enhances the readout SNR by nearly an order of magnitude.

$$P_N = k_b T_N \triangle f \tag{3.1}$$

There will be noise P_N in the system from sources such as JPA and analog components, and voltage sources that will affect the overall system. However, white noise, also known as Johnson-Nyquist noise, is a common contention for evaluating SNR, whose primary contributions come from the temperature and signal generators to the system. When the system has a higher noise temperature T_N, this results in a higher noise floor in our demodulated RF signal spectrum P_N. In the setup used, T_N

is mostly dominated by the Linear Amplifier in the second mixer stage with a noise of 5 K, but when readout with JPA is performed, the SNR is improved by tenfold with the JPA only contributing 0.1 K noise when enabled. [43]

Another factor is the bandwidth $\triangle f$ of the UHF-LI demodulator filter. The low-pass filter was set with a cutoff frequency of 26 kHz to see only up to 10^4 Hz. As we increase the bandwidth, thus decreasing the integration time τ in Figure 3.3, the plots become noisier. Additionally, we see the much improved SNR when the JPA is turned on. By averaging multiple Fourier spectrums of the demodulated signal amplitude Γ, the SNR can be estimated by

$$SNR = [\frac{\delta\Gamma}{\delta C} \triangle C]^2 \frac{P_{input}}{P_N} \tag{3.2}$$

This equation describes how the SNR is affected in terms of a change in the demodulated amplitude Γ with respect to a change in capacitance C. Once a Coulomb peak is mapped, the gate voltage is fixed at the steepest point because it correlates with the highest change in capacitance, $\triangle C$. In addition, in this work, we find that the input RF carrier signal, P_{input}, has a linear relationship with the SNR.

3.2 Reflectometry on Double Quantum Dot device and stability diagram

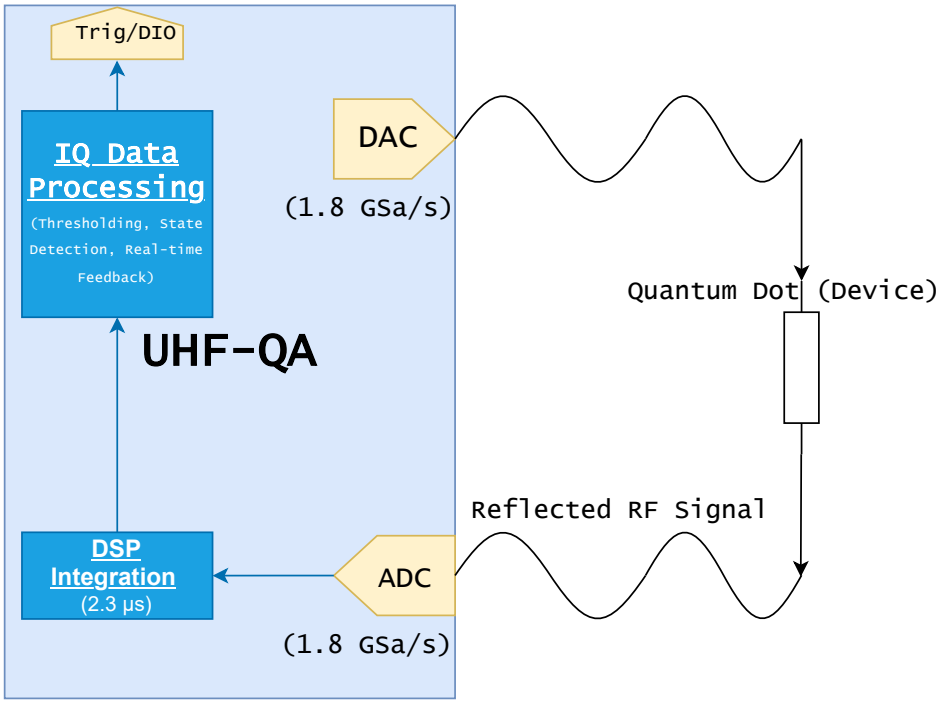

Figure 3.4: Simplified schematic illustrating the UHF-QA signal processing path used for Quantum Dot reflectometry experiments. The reflected RF signal is digitised at 1.8 GSa/s, integrated over a user-defined 4096-sample window ($2.3\mu s$), and produces IQ values used for state discrimination and triggering via the DIO interface. [5]

From figure 3.1 which show the Sample, the gates G_2, G_3, and G_4 exist at the 6 mK stage of the dilution refrigerator: see Appendix B, these gates are connected through the DC lines, highlighted in blue dashed lines, and these DC signals are connected to room temperature signal supplies such as the UHF instrument's DC outputs.

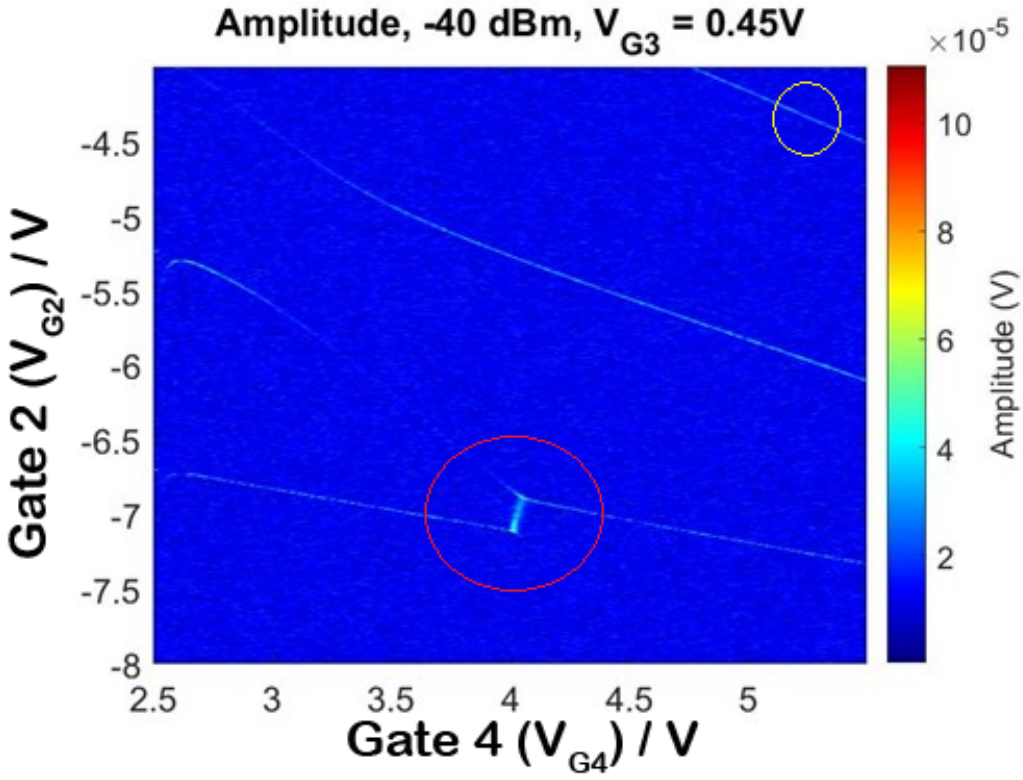

Figure 3.5: Mapping of the Coulomb diamonds present with two gate voltages - double Quantum Dot feature found circled in red, single electron movement in yellow

We fix the voltage to G_3, and vary the voltages applied to gates 2 and 4 and plot the response, seen in above figure 3.5. the x-axis (Gate 4, V_{G4}) is supplied by the UHF-LI Auxiliary Output and the y-axis (Gate 2, V_{G2}) is provided by the UHF-LI Signal Output. The yellow circle area at the top right represent single charge detection: the movement of a single electron on and off the Quantum Dot. The red circle area is the double Quantum Dot area of interest: where an electron moves between the two dots by varying the voltage. By zooming into this area of interest, we can more clearly see this tunnelling region below in Figure 3.6.

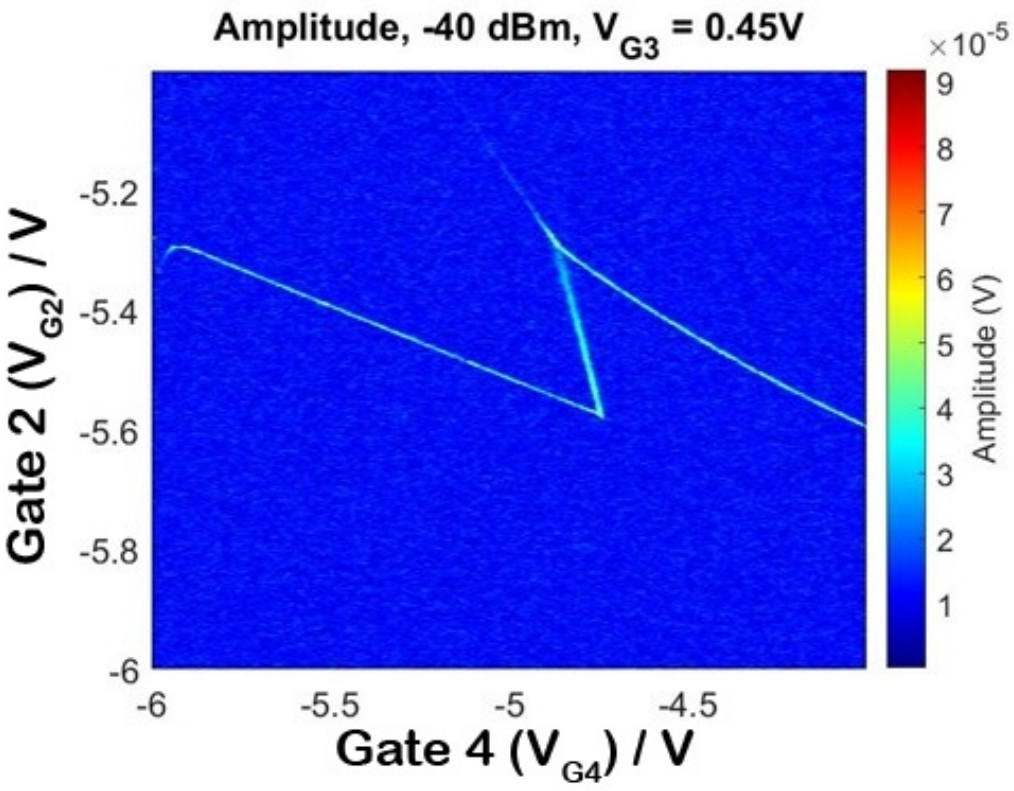

Figure 3.6: Zoom into the DQD region circled in red from Figure 3.5 with smaller voltage ranges and higher voltage step resolution. This sets up the operating point for further experiments as seen in Figure 4.1

By changing the gate voltages G_2 and G_4, one can map out the stability diagram of a QD which assumes the shape of a series of diamond-shaped regions, the Coulomb diamonds.

3.3 Summary of Charge State Measurements

- Tuned the device to single-dot and double-dot regimes and mapped charge stability diagrams using RF reflectometry.
- Quantified the benefit of the cryogenic amplification chain by measuring SNR as a function of integration time and RF power (with/without JPA).
- Demonstrated high-contrast detection of dot–lead and interdot transitions; identified honeycomb structure and triple points consistent with a DQD.
- Established acquisition settings (demodulation bandwidth, dwell times, step

sizes) that balance scan speed against energy resolution and noise.

3.4 Discussion and Results

The measurements in this chapter validate the readout strategy on an actual sample device: reflectometry cleanly resolves both dot–lead and interdot transitions with short integration, and the validation of JPA amplifying readout times with much higher SNR values of demodulated amplitude in the range of 60 μV with integration times set to 10 μs. The stability diagrams exhibit the expected slopes and curvature from cross-capacitances and tunnel coupling, confirming independent gate voltage control and sweeps accurately shows independent control of charge occupancy and detuning. Where bias spectroscopy is available, lever arms and charging energies can be extracted quantitatively which will be discussed more in the paper to be published "Radio-frequency readout of ultra-low noise carbon nanotube quantum dot devices" by Ravichandar et al.

Overall, Chapter 3 translates the Chapter 2 toolbox into device parameters and measurement settings that the time-domain control in Chapter 4 can build on.

Chapter 4

Microwave Pulsed Spectroscopy on Quantum Dot Charge Qubits

4.1 Charge Qubit Spectroscopy

Before we perform pulsed experiments, it is essential to establish the two-level system behavior of the Charge Qubit. This is achieved through microwave spectroscopy. Figure B.1 shows the practical setup of a DQD sample hosted in a dilution refrigerator.

4.1.1 Theory behind energy detuning and quantum capacitance relation

The M8195A output is connected to a microwave line connected to G_4, denoted in Appendix B Figure B.1 as 1., and set to 0 V DC offset. The 2D stability diagram is captured as seen in Figure 4.1, with the left gate (vertical axis) $V_{G2} = -5.65V$, and the right gate (horizontal axis) V_{G4} swept across the level detuning.

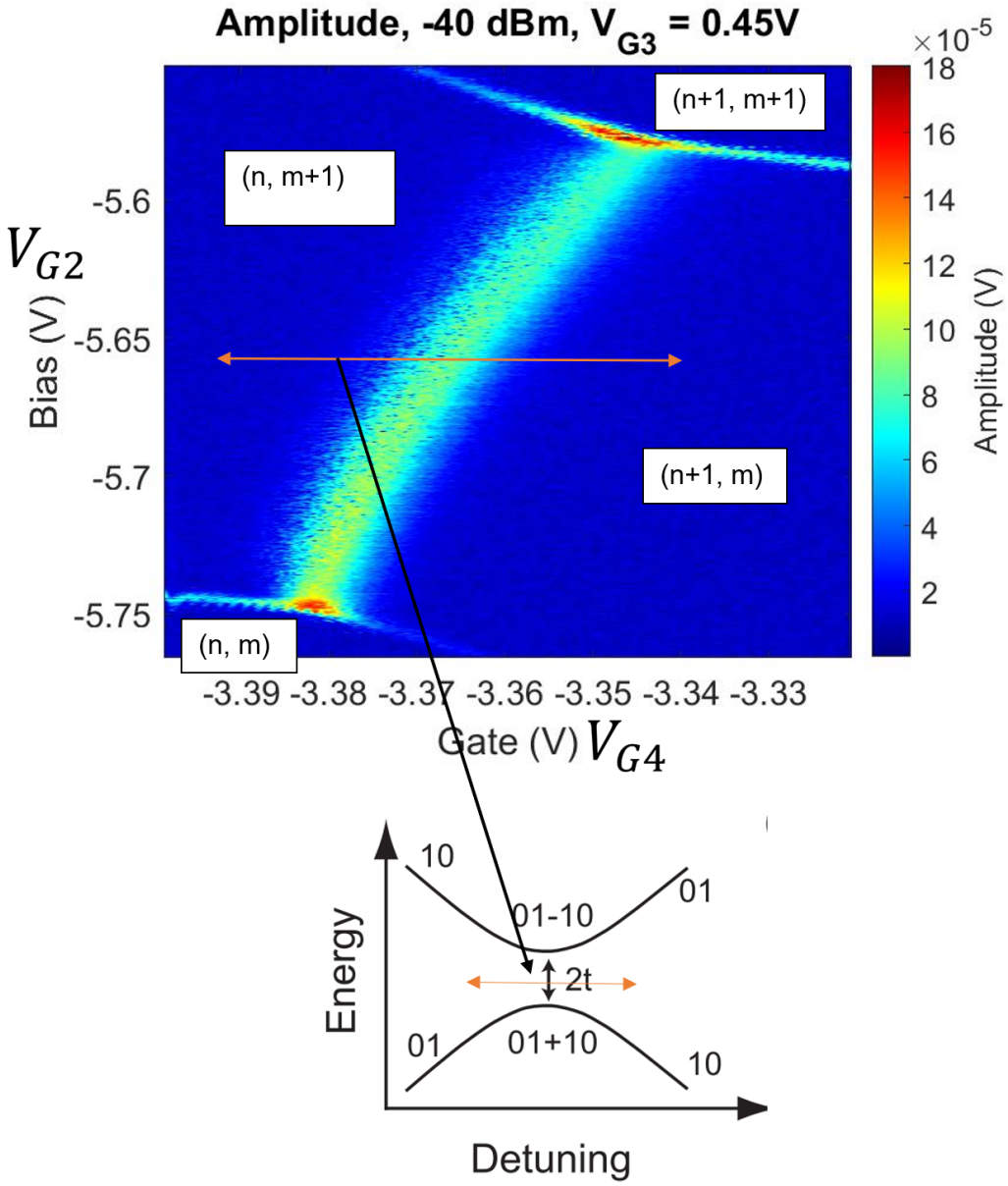

Figure 4.1: The detuning line from a stability diagram and energy scale diagram, the charge stability diagram is obtained by sweeping the gate voltages: V_{G4} captioned Gate (V) and V_{G2} captioned Bias (V), with fixed $V_{G3} = 0.45V$. (n,m) denotes n for the number of electrons on the left dot, and m for the right dot.

The resonance frequency is when the qubit state is resonantly driven between the ground and the excited state; $|01-10\rangle$ and $|01+10\rangle$ in the case of Charge Qubits. At zero detuning, the energy that separates both states is $2t_c$ where t_c is the tunnel coupling and the further away from zero detuning, the state splitting increases.

$$H = \frac{1}{2}\varepsilon\sigma_z + t_c\sigma_x \tag{4.1}$$

ε is detuning as the difference in energy levels on the x axis of Figure 4.1. This is different to the frequency detuning Δ which we expand further later. During detuning $\varepsilon = 0$, the difference in spacing between the two dots t_c, where the energy levels of ground and excited state of the qubit are mixed into the superposition state quantified by eq. 4.2.

$$E_{\pm} = \pm\frac{1}{2}\sqrt{\varepsilon^2 + (2t_c)^2} \tag{4.2}$$

At $\varepsilon = 0$ the qubit frequency is $\omega_q = 2t_c/\hbar$. As described by eq. 4.2, $E_{\pm}$ is the energy difference of the excited and ground states which corresponds to the qubit's transition energy. This level is related to the capacitance of the read-out resonator eq. 4.3 coupled to the DQD. The change in capacitance directly relates to the phase shift of the RF response from the DQD readout. Associating the demodulated phase or amplitude with the qubit's state energy level allows averaging the qubit state probability over many measurements and plotting it. [41] [2]

$$C_Q^{\pm} = -(\varepsilon\kappa)^2\frac{\partial^2 E_{\pm}}{\partial^2\varepsilon} \tag{4.3}$$

Equivalently, by the assumption that the coupled resonant circuit is related to the state of the Charge Qubit, the quantum capacitance of the system can be derived eq. 4.3. This equation demonstrates the quantum capacitance of the qubit state as a function of its band curvature or polarization. When $\varepsilon = 0$, the capacitance is given by eq. 4.4. κ (eV/V) is the lever arm of the gate that quantifies the coupling strength between the resonator and the energy levels of the qubit: it is the conversion of a

change in gate voltage into an energy shift in the qubit state.

$$C_Q^{\pm}(\varepsilon = 0) = \mp \frac{1}{2} \frac{(e\kappa)^2}{2t_c} \tag{4.4}$$

Equation 4.3 relates the quantum capacitance $C_Q^{\pm}$ to the curvature of the energy band of the qubit $\frac{\partial^2 E_{\pm}}{\partial^2 \Delta}$. Equation 4.4 is when evaluated at zero detuning, $C_Q^{\pm}$ depends inversely on tunnel coupling t_c, the energy splitting. This relationship is used experimentally to extract C_Q from the measured phase shifts and, in turn, to infer key device parameters such as t_c and κ.

4.2 Rabi oscillation

Rabi oscillations demonstrate coherent control of a qubit's state throughout resonant microwave pulses. We first performed theoretical simulations to predict the expected Rabi oscillation behaviors, which serves as a guide for future experimental design. The purpose of these experiments is to measure key parameters, including Rabi frequency Ω_R, rotation times (T_π and $T_{\frac{\pi}{2}}$), coherence properties and Rabi quality factor Q. The Rabi quality factor quantitatively relates the coherence time of Rabi oscillations (T_2^{Rabi}) to the rotation time of a π-pulse (T_π), providing information on the performance of the qubit: [44]

$$Q = \frac{T_2^{Rabi}}{T_\pi} \tag{4.5}$$

Precisely tuning the microwave frequency ω_d to match the qubit's resonance ω_q ensures efficient state rotations, while increasing the pulse amplitude reduces rotation times since the Rabi frequency Ω_R scales linearly with the microwave amplitude $\Omega_R \propto A$, assuming resonant drive.

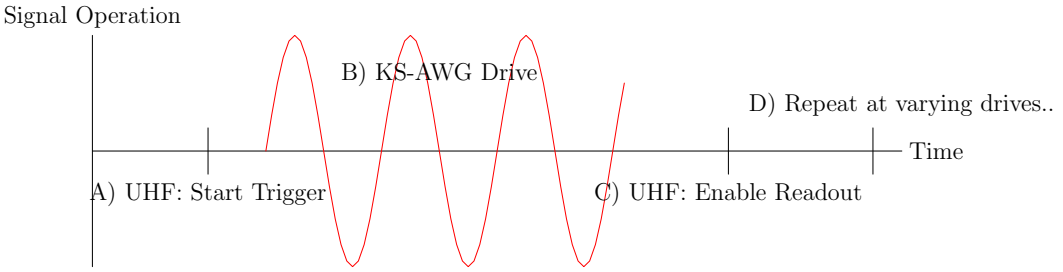

Figure 4.2: Rabi control pulse scheme. (A) UHF-QA sends the initial trigger. (B) KS-AWG (M8195A) drives the qubit for a varying pulse width. (C) UHF-QA begins readout and demodulation at the end of the pulse duration. (D) The sequence is repeated with different drive parameters such as Pulse Width or Amplitude to observe Rabi oscillations.

Figure 4.2 illustrates the control sequence used:

(A) : An initial trigger from the UHF-QA starts the experiment.

(B) : Microwave pulses of variable duration or amplitude are generated by the M8195A.

(C) : The UHF-QA records the qubit state immediately after pulse application.

(D) : The sequence repeats to capture coherent oscillations of the population in the qubit state.

4.2.1 Simulation

4.2.1.1 System Hamiltonian

To predict experimental outcomes, numerical simulations were conducted using a hybrid Qiskit-QuTiP framework. The qubit dynamics under microwave driving is described by the Hamiltonian:

$$H = \frac{\Delta}{2}\sigma_z + \frac{\Omega_R}{2}\sigma_x \tag{4.6}$$

Individual contributions are defined as follows:

$$H_{\text{detuning}} = \frac{\Delta}{2}\sigma_z \qquad \text{(Detuning)} \tag{4.7}$$

$$H_{\text{drive}} = \frac{\Omega_R}{2}\sigma_x \qquad \text{(Drive Hamiltonian)} \tag{4.8}$$

The Hamiltonian explicility includes the time-dependent microwave drive term, placing our simulation employing the rotating-wave approximation (RWA). We employ the full lab-frame Hamiltonian to fully capture high-frequency drive dynamics, which is important for realistic experimental modeling. Here, the detuning Δ is set to zero for resonance, Ω_R is the Rabi frequency, and σ_x, σ_z are Pauli operators. [45]

Ω_R : Rabi frequency rad/s

Δ : Detuning between qubit frequency ω_q and drive frequency ω_d

ω_q : Qubit's resonance frequency

ω_d : Microwave drive field frequency

σ_z, σ_x Pauli-Z and Pauli-X operators

The Hamiltonian captures the essential dynamics of the DQD under coherent drive: detuning shifts with energy levels, tunnelling mixes the charge states, and the external microwave pulse induces oscillations between them.

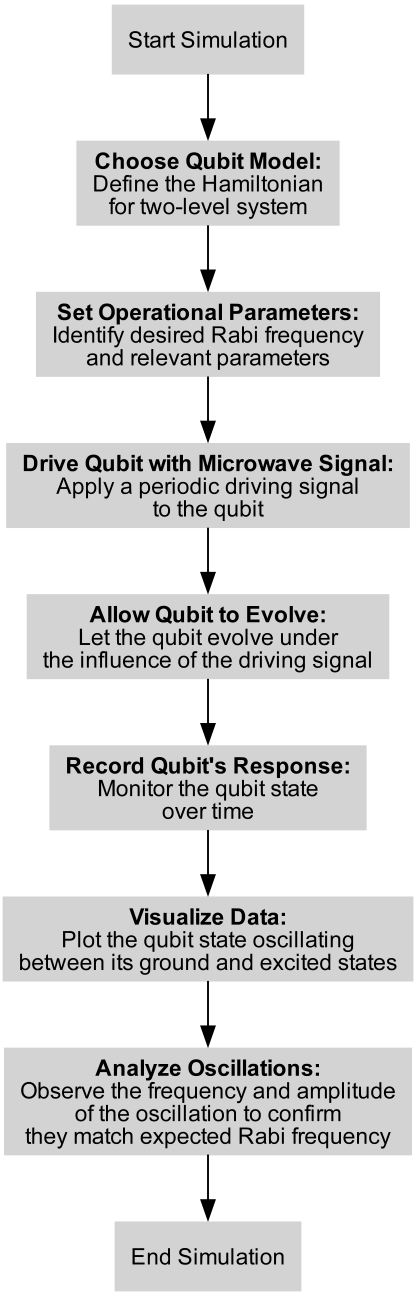

Figure 4.3: Conceptual flowchart outlining the steps to simulate Rabi oscillations in a double Quantum Dot Charge Qubit, highlighting the progression from system selection to the final analysis of oscillatory behaviour. Operational parameters such as Rabi frequency are optimized, and the qubit's evolution is driven by a microwave signal, with data visualization providing insights into the qubit's response over time.

4.2.1.2 Simulation parameters

The simulation parameters are consistent with typical measurement parameters:

Rabi frequency angular (Ω_R) :	1.428 GHz
Drive frequency (ω_d) :	1.148 GHz
Total simulation time :	500 ps
Detuning (Δ) :	0 (resonance)

These parameters were selected to resemble the real physical conditions in the laboratory, allowing for qualitative comparison between simulation and experimental data. The simulation outputs the qubit's state evolution on the Bloch sphere and enables visualisation of coherent Rabi oscillations.

4.2.1.3 Simulation results and analysis

Figure 4.4 shows the simulated Rabi oscillations, clearly demonstrating coherent oscillations between the ground and excited states at the chosen Rabi frequency.

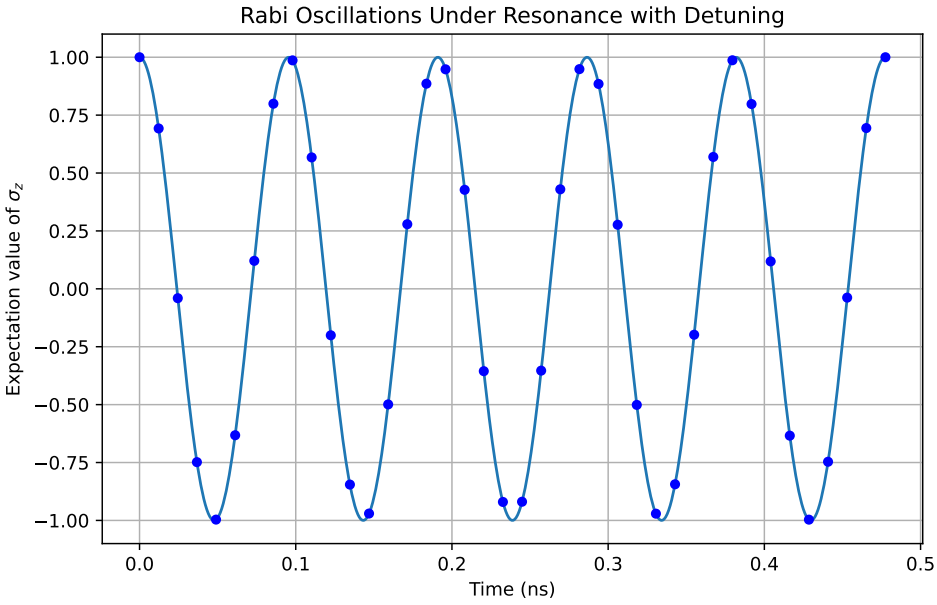

Figure 4.4: Simulation of Rabi oscillations using the QuTiP solver. The expectation value of σ_z oscillates as a function of drive time under a resonant microwave field. This reflects coherent population exchange between the ground and excited states of a two-level system.

The Rabi oscillation simulation shows coherent population transfer between the two qubit states under resonant microwave driving. From the initial simulation before using the QuTiP solver, the Rabi period T_{rabi} was set to 0.7 ns and it can be confirmed by extracting the frequency from Figure 4.4 that it matches the desired Rabi frequency: validating the simulation given our initial parameter. We see in this figure the expectated behaviour of a two-level system which is driven under no dephasing or relaxation.

4.2.2 Experimental Setup and Timing

A physical loopback test (Figure 4.5) is tested to validate instrument timing and pulse synchronisation. The test synthesizes 100 Gaussian pulses from the M8195A into the UHF-LI, generating three trigger stages per pulse.

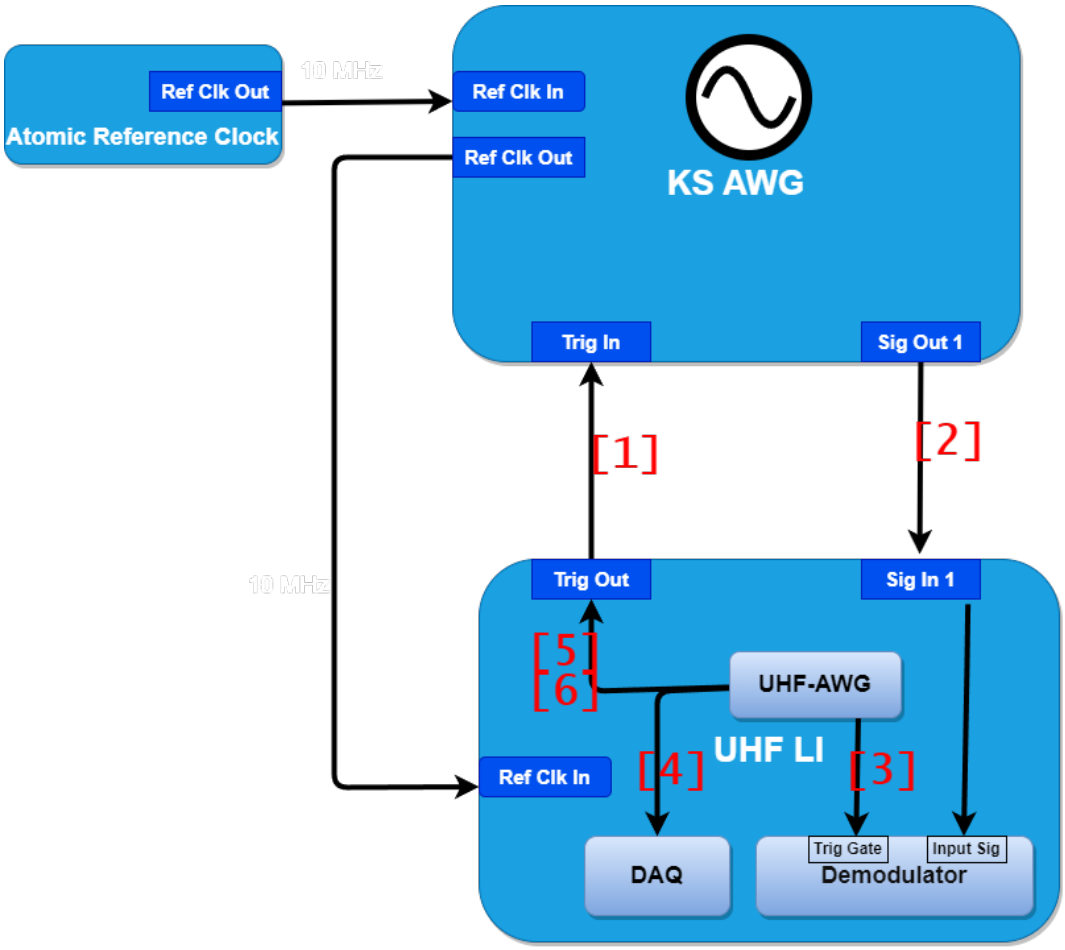

Figure 4.5: Rabi sanity test in denoted order [1] Send first trigger to initiate [2] Generates Gaussian pulse [3] Trigger Demodulator to capture [4] Trigger DAQ to plot captured data [5] Turn all triggers off [6] Repeat step 1

4.2.2.1 Gaussian pulse sweep

This functional form was chosen to model a decaying Rabi envelope with oscillations corresponding to an assumed Rabi period. This approach validated that the UHF demodulator correctly reconstructs Rabi oscillations when synchronised with a known amplitude pattern. No DQD device is connected in this test; the goal is validating demodulation timing and UHF-DAQ synchronisation.

$$\text{Gauss Amplitude(x)} = A_0 \cdot e^{\frac{-x}{\tau_{decay}}} \cdot cos(\frac{2\pi x}{RabiPeriod}) \tag{4.9}$$

Where x is the pulse-sequence index 1 to 100. The chosen Rabi frequency for this experiment was 1.428 GHz, corresponding to a Rabi oscillation period of 0.7 ns,

and thus defined the synthesized Gaussian pulse period. Equation 4.9 is a Gaussian amplitude decay function that artificially resembles Rabi oscillations [46]. The decay constant ($\tau_{decay} = 100$ ns) was empirically selected based on the coherence times observed in similar DQD experiments, representing a reasonable estimate for our experimental setup.

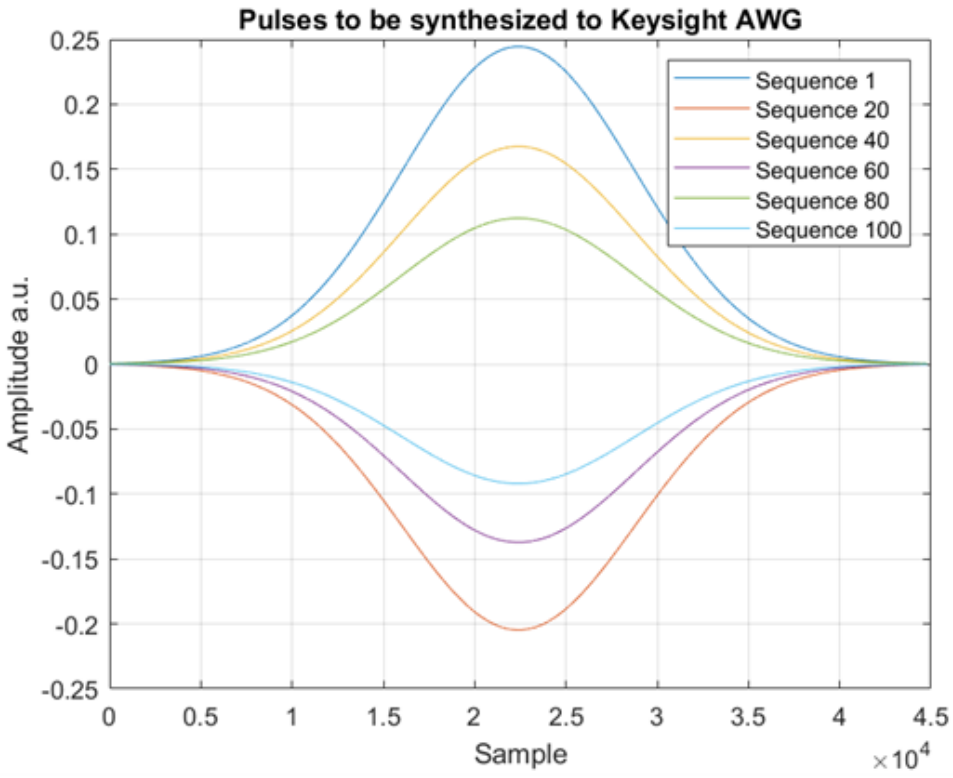

Figure 4.6: Representative Gaussian pulse shapes uploaded to the AWG for synthesising experimental Rabi oscillations.

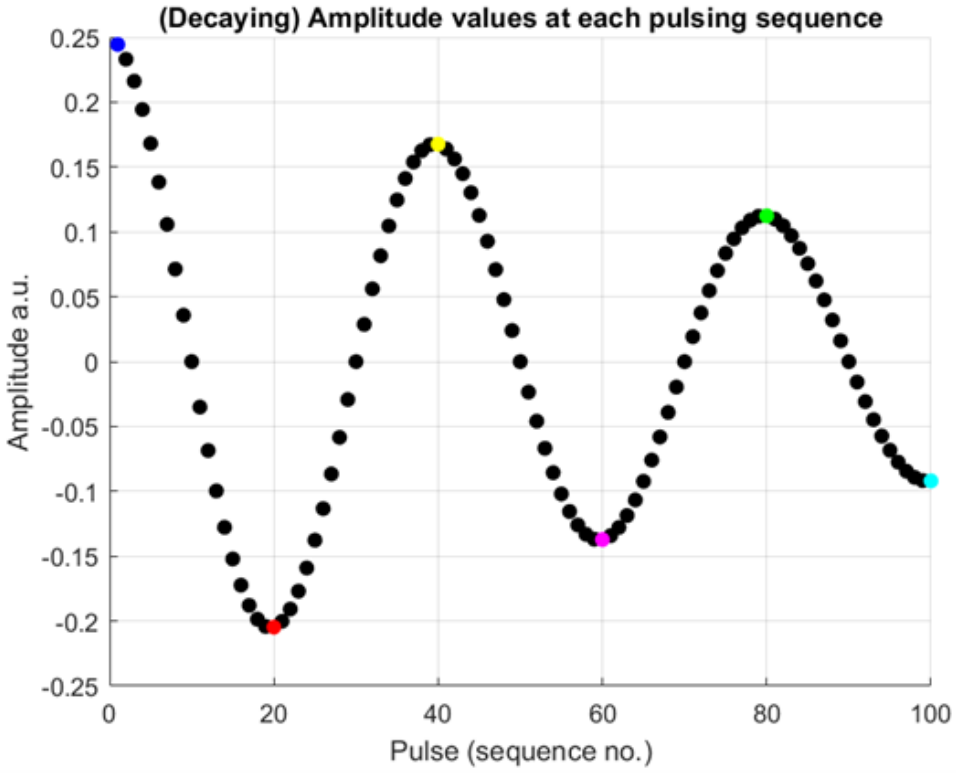

Figure 4.7: Gaussian pulse amplitude y-axis with arb. unit values for each of the 100 pulse sequences, on the x-axis, synthesising a decaying Rabi oscillation envelope to validate demodulation and timing synchronisation.

The UHF demodulator in figure 4.8 shows a one-time trace capture of $1.6\mu s$ with the Gauss waveform detected in $V_s(t)$. The quadrature output signals X, Y in (a) are connected to the UHF-DAQ module. The demodulator outputs at 14.07 MSa/s; one data point every 71.07 ns is sent to the DAQ, which is set to capture 22 data points, which is $\approx 1.6\mu s$ (y-axis in Figure 4.9). After repeating for the 100 pulse sequences, a 2D plot is shown in Figure 4.9. In future experiments with the measurement connected to a DQD, the oscillation function can be fit along the line trace to find the Rabi frequency of our system.

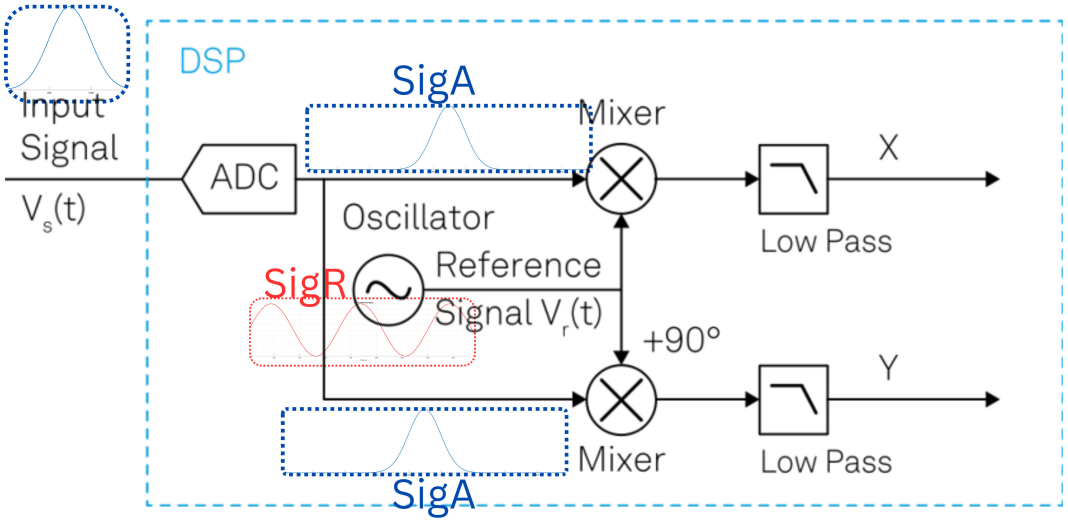

(a) UHF-LI demodulator: one capture sequence

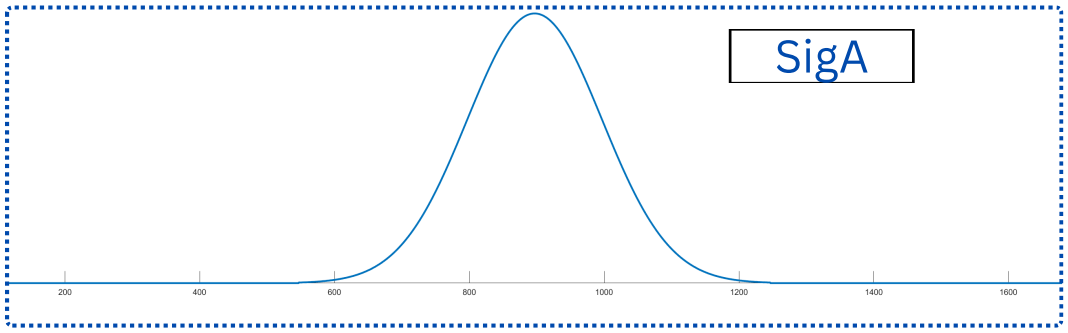

(b) UHFLI Input digitised signal: a Gaussian waveform

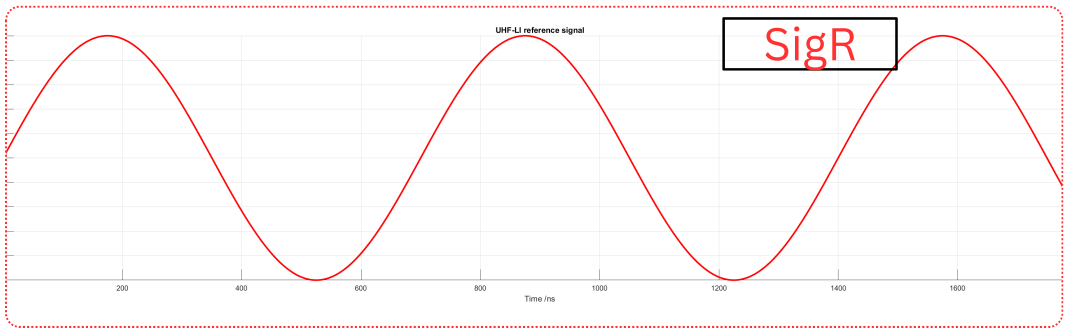

(c) Internal reference signal $V_r(t)$ of 1.4 MHz

Figure 4.8: a) Functional diagram of the UHF-LI demodulation with the two signals *SigA* (blue) and *SigR* (red) captured on a trigger detection event. After mixer stage, a low-pass filter is set with a time-constant $\tau_{TC} = 49ns$. b) UHF-LI Input Signal $V_s(t)$, labeled *SigA*, time trace capture in ns-timescale, Gauss signal detected c) Reference Signal $V_r(t)$, labelled *SigR*: the internal UHF-LI reference used at the mixer stages.

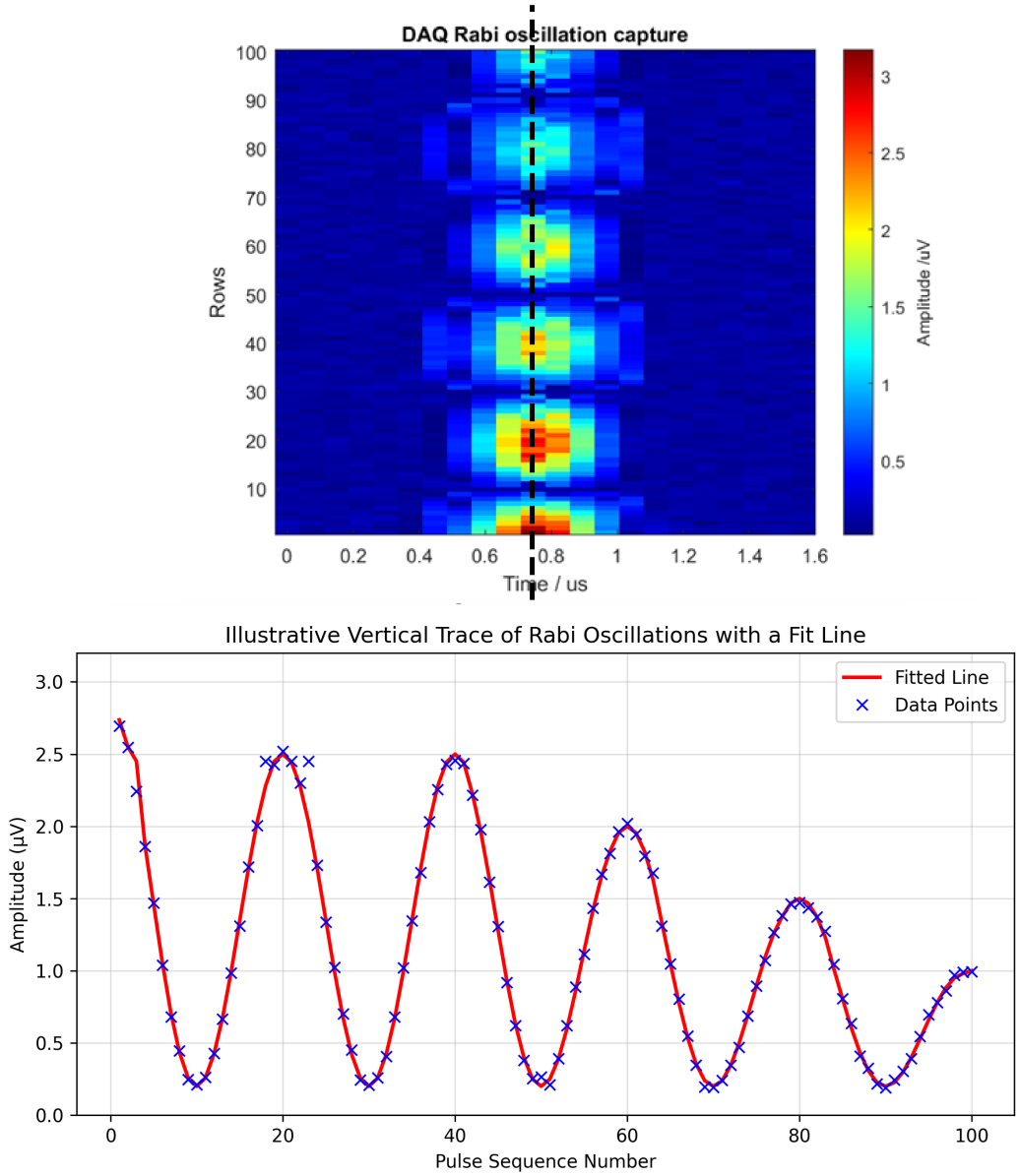

Figure 4.9: (Upper Panel) Demodulated amplitude map for synthesized Gaussian pulses, clearly displaying coherent oscillations across 100 pulse sequences. The black dashed vertical line at approximately $0.8\mu s$ indicates the extraction point used for further analysis. (Lower Panel) Extracted vertical trace demonstrating the characteristic decaying envelope of Rabi oscillations. Scatter points represent measured amplitude values, and the solid line is a fitted curve, validating the synchronisation and timing accuracy of the experimental setup.

If we take a vertical line trace at 0.8μs, we can observe a similar decaying oscillation behavior modeled for the Gaussian amplitudes in Figure 4.7. The vertical trace at $0.8\mu s$ was selected as representative due to its clear demonstration of coherent oscillatory characteristics, as expected from Figure 4.7. A sine fit with the demodulated amplitude vs. pulse sequence number (x-axis rows) in Figure 4.9 yielded a Rabi frequency of approximately 1.428 GHz, consistent with the simulated Rabi-like Gaussian pulses from Figure 4.9 supporting the claim of validating UHF demodulation.

More importantly, the simulation aimed to demonstrate the control loop and feedback loop and measurement setup. This allows characterizing timing uncertainties, jitter, skew, and amplitude. The timing certainty that each Gauss signal is integrated at a reliable time with a peak around $0.8\mu s$. The total time to perform 100 amplitude oscillation measurements with a measurement averaging just one was 160 *ms*, which can be further experimented with the UHF-LI alternative UHF-QA.

4.2.3 Quantitative Analysis of Rabi Oscillations

- π-pulse duration (T_π):

$$T_\pi = \frac{\pi}{\Omega_R} = \frac{\pi}{2\pi \times 1.428\ \text{GHz}} \approx 350.14\ \text{ps} \tag{4.10}$$

- The Gaussian envelope decay constant was calculated with $\tau_{decay} = 100$ ns, the coherence time can be approximated as:

$$T_2^{Rabi} \approx \tau_{decay} = 100\ \text{ns} \tag{4.11}$$

- Rabi Quality Factor Q:

$$Q = \frac{T_2^{Rabi}}{T_\pi} = \frac{100\ \text{ns}}{350.14\ \text{ps}} \approx 285.6 \tag{4.12}$$

This derived Q factor ≈ 285 is comparable to typical charge-qubit coherence values reported in the literature, demonstrating robust coherence under our experimental conditions and a synthetic τ_{decay}. These quantitative results verify our control

setup and highlight the capability to achieve high-fidelity state manipulation using the developed instrumentation.

4.3 Ramsey Interferometry experiment

While Rabi oscillations reveal the qubit's controllability, Ramsey interferometry provides a direct measure of phase coherence and sensitivity to detuning noise. We example the implementation of a Ramsey sequence by simulating this experiment and extract the coherence time T_2^*: the phase coherence via interference between time-evolved qubit states. [47]

4.3.1 Ramsey pulse sequence

In this experiment's pulse sequence, an initialised qubit is subjected to the first $\frac{\pi}{2}$ pulse to let it evolve freely for a specified delay time τ, before the second $\frac{\pi}{2}$ pulse is applied. Following the second pulse, a readout procedure probes the phase response of the qubit, and hence the resultant state. The experiment occurs at zero detuning $\Delta = 0$; two $\pi/2$ pulses are applied with a variable waiting time (τ) between, averaged many times at each point in the detuning axes.

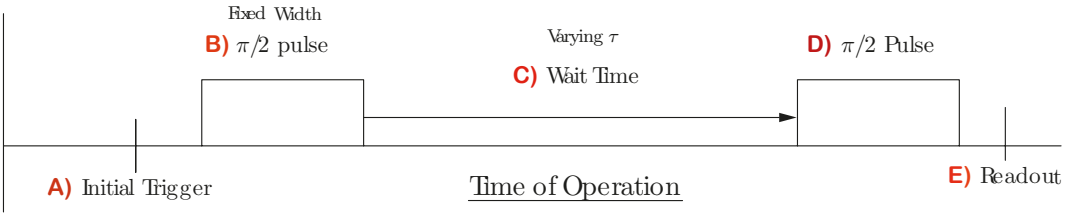

(a) Ramsey pulse timing sequence

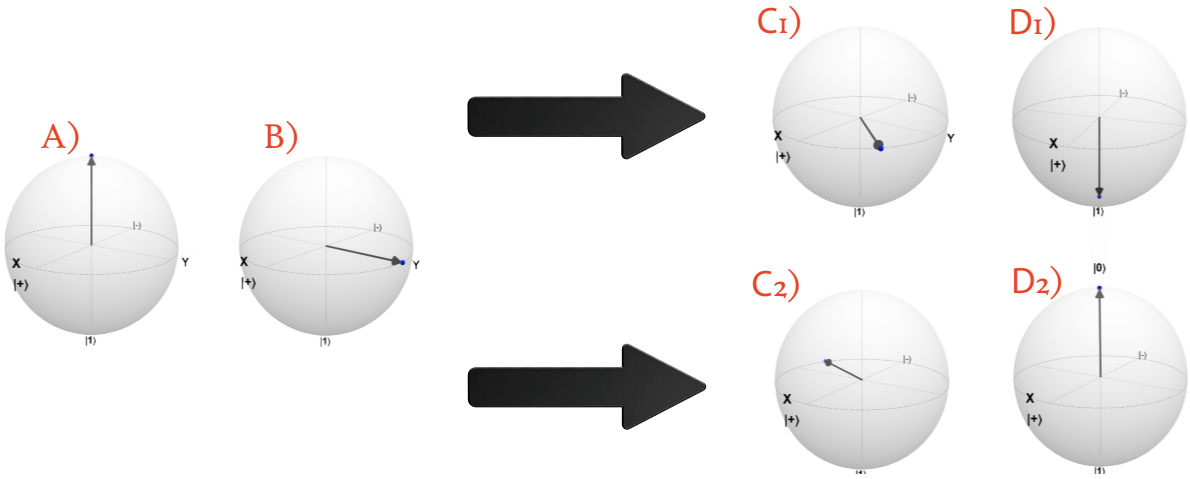

(b) Ramsey Bloch sphere sequence

Figure 4.10: Bloch sphere diagrams showing qubit evolution through the Ramsey sequence: A) initial state, B) after the first $\frac{\pi}{2}$, C) free evolution, and D) final state measurement.

1. The qubit is initialised to the state $|0\rangle$
2. A $\frac{\pi}{2}$ pulse rotates the qubit around the x-axis to the equator as seen in the Bloch sphere
3. During the delay time τ, the qubit freely evolves and processes around the z-axis
4. Another $\frac{\pi}{2}$ pulse is applied rotating the qubit by another 90*, which now maps the y-axis onto z-axis
5. Measuring and demodulating the readout signal shows the phase response: also the final state of the qubit, which can be in $|0\rangle$ or $|1\rangle$
6. The change in phase difference is plotted at the different delay times, which should exhibit an exponential decay fit

4.3.2 Ramsey Experiment Simulation

The simulation involves modeling the qubit's Hamiltonian using the same Hamiltonians as from Rabi simulation eq. 4.6. We apply the Ramsey pulse sequence and calculate the final state population. The chosen parameters for the simulation were based on experimental observations of the qubit system and are as follows:

ω_Q	1.148 GHz
Ω_R	1.428 GHz
$\frac{\pi}{2}$ Pulse Duration	$\approx$ 175.07 ps
Δ Detuning	Set to 0 to simulate on-resonance
γ Decoherence Rate	25 MHz: based on realistic coherence $T_2^* times$
τ_{decay} Decay constant	100 ns

This approach simplifies experimental setups by removing the need for fine-tuning of microwave frequencies. A typical decay rate of $\gamma \approx 25$ MHz, corresponding to $T_2^* \approx 100$ ns, is consistent with experimental values in semiconductor Charge Qubits. [19]

The simulated Ramsey fringes accurately represent the phase coherence dynamics other experimental systems similar to the system in lab, allowing for effective extraction of the coherence time T_2^*. The simulation code calculates the qubit's state at each step of the Ramsey sequence and extracts the final-state population. Repetition of the simulation for different free evolution times (τ), the characteristic Ramsey fringes can be observed, and the decay of these fringes provides information on the decoherence time of the qubit T_2^*.

$$T_{\frac{\pi}{2}} = \frac{\pi}{2 \times \Omega_R} = \frac{\pi}{2 \times 2\pi \times 1.428\ \text{GHz}} \approx 175.07\ \text{ps} \tag{4.13}$$

The pulse width $\frac{\pi}{2}$ is modeled as square pulses with a duration determined by the Rabi frequency (Ω_R) in the equation 4.13. The free evolution period is governed by the static Hamiltonian (H_Q). The simulation code computes the qubit's state at each step of the Ramsey sequence and extracts the final-state population. By repeating the

simulation for different free evolution times (τ), we can observe the characteristic Ramsey fringes, which are oscillations in the final population as a function of τ. The decay of these fringes provides information about the qubit's decoherence time (T_2^*). In a practical experiment, decoherence arises from interactions with the environment, leading to a loss of coherence in the qubit's state. By simulating the Ramsey experiment, we can gain insights into the qubit's behavior and optimize the experimental parameters to achieve better coherence and control.

4.3.2.1 Measuring relaxation time

In order to demonstrate the simulation of decoherence noise and find T_2^*, we use the addition of the scipy module in Python. For different free evolution times τ, the expectation value σ_z is recorded and then plotted. T_2^* is found by fitting the curve according to a decay function we define in eq. 4.14

$$f(t) = Ae^{\frac{-t}{T_2^*}} \cos(\omega t + \phi) + C \tag{4.14}$$

Parameter	**Meaning**	**Value**
A (Amplitude)Amplitude	Initial oscillation amplitude	0.5
t	Time delay between $\frac{\pi}{2}$	0 to 300 ns, 300 steps
ω	Oscillation frequency (typically related to detuning Δ)	25 MHz
ϕ	Phase offset	0
C	Vertical offset or average population baseline	0.5

Table 4.1: Fitting function parameters

Figure 4.11 shows Ramsey fringes that decay over time due to phase decoherence, consistent with T_2^*.

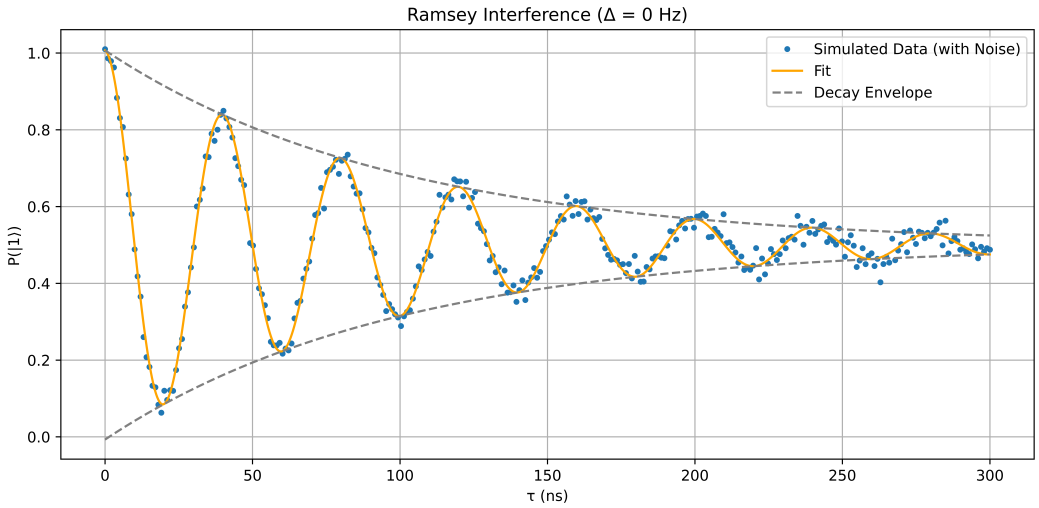

Figure 4.11: Simulated Ramsey signal and fit: simulated Ramsey interference data (blue dots) with fitted decaying sinusoidal curve (orange line) used to extract the qubit coherence time T_2^* to be 99.26 ns. The gray dashed lines show the decaying envelope bounds $\pm Ae^{\frac{-t}{T_2^*}} + C$, highlighting the loss of phase coherence over time.

The dephasing noise injected into the Ramsey signal at τ is given by

$$P_e(\tau) = \frac{1}{2} + \frac{A}{2} \left\langle \cos\left[(\omega + \delta\omega(t))\,\tau + \delta\phi(\tau)\right] \right\rangle + C \tag{4.15}$$

where $\delta\omega(t)$ represents frequency fluctuations (drive/qubit detuning noise) and $\delta\phi(\tau)$ captures residual LO/AWG phase jitter accumulated between the two $\pi/2$ pulses. This dephasing noise is modeled as frequency jitter of the qubit during the free-evolution interval. For each delay τ, we add a Gaussian phase noise $\phi \approx N(0, \sigma_\phi^2(t))$ with $\sigma_\phi^2(t) = \frac{2\tau}{T_2^*}$. This yields the envelope $e^{\frac{-t}{T_{2**}}}$ used in the fit in the above figure. We set $T_2^* = 99.26ns$ from the fit, derived from the diffusion rate $D = \frac{1}{T_2^*} = 1.01 \times 10^7 s^{-1}$. Independent noise was added at $\sigma_{meas} = 0.02$ (fraction of full scale) to simulate readout noise.

4.3.3 Ramsey practical implementation

In the setups shown in figures B.1 and 3.1, G_2 and G_4 are used to control tunnel coupling and detuning between dots, the gate G_4 will be pulsed for detuning variation

to modulate the potential between dots during the Ramsey delay period. This allows for initialisation and readout at a fixed anti-crossing. The readout signal is demodulated or integrated in step E) of Figure 4.10, giving us phase ϕ. By averaging many measurements, the population of the qubit state is plotted as a function of the wait time C).

The UHF-QA will generate a continuous RF signal from the signal output to the resonator at the source electrode, typically in the 560-590 MHz range. With the resonant microwave frequency from the Rabi oscillations chapter for state transitions, the same M8195A will send a $\frac{\pi}{2}$ pulse, and a variable waiting time τ will be added [44]. The wait time of the experiment is the dependent parameter, ranging from 10 ns to 100μs.

The first $\frac{\pi}{2}$ microwave pulse will excite the qubit, and then the wait time τ will allow the qubit to freely evolve until the second $\frac{\pi}{2}$ pulse rotates the qubit further. If the wait time τ is too short, the qubit will have no time to relax, and the demodulated phase difference will be close to the background level. If the difference is too high, the amplitude of the demodulated phase signal will approach half the amplitude of the background phase at thermal equilibrium [48].

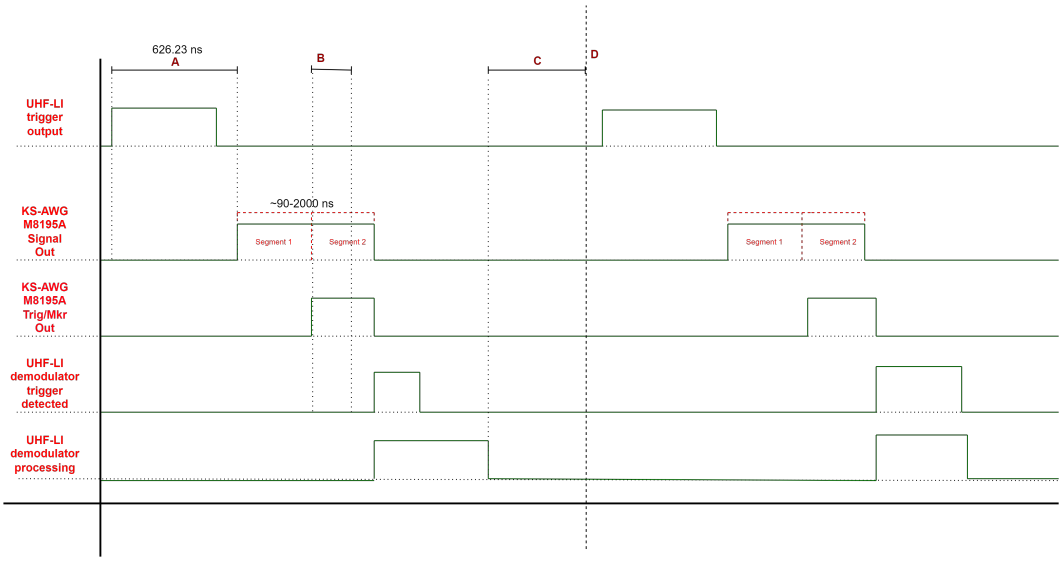

Figure 4.12: Ramsey Pulse control timing diagram with each step notated from A to D

The experiment begins with the UHF-LI sending a signal from its Trigger Output 1 port connected to the Keysight M8195A Trigger input, enabling the M8195A to

output a combined burst of two waveform segments to the plunger gate G_4 of the Double Quantum Dot. Figure 4.12 shows the initial start of the experiment, the marker D is the separator between each iteration with a different waiting time in the segments. Segments 1 and 2 comprise the first half of the pulse sequence: the first segment contains the pulse $\frac{\pi}{2}$ along with the waiting time, and the second has the second pulse $\frac{\pi}{2}$. Along with segment 2 in parallel, another segment is designed to play from the trigger output at the same playback time as segment 2 occurs, and this trigger output is connected to the UHF-LI Trigger Input 2. The UHF-LI demodulator trigger source is set to Trigger Input 2. So once this trigger is detected after a small delay, it enables the UHF-LI to begin processing the demodulator and sort the demodulated phase samples, before sending them to the PC for plotting and data analysis. The initial trigger is seen in figure 4.12.

Following the rules of microwave signal generation from Section 2.2, using the maximum synthesise value of the 65 GSa/s DAC sample rate is ideal to step τ with the lowest possible values for the highest signal clarity, as low as lowering to the 154 ps period between each sample.

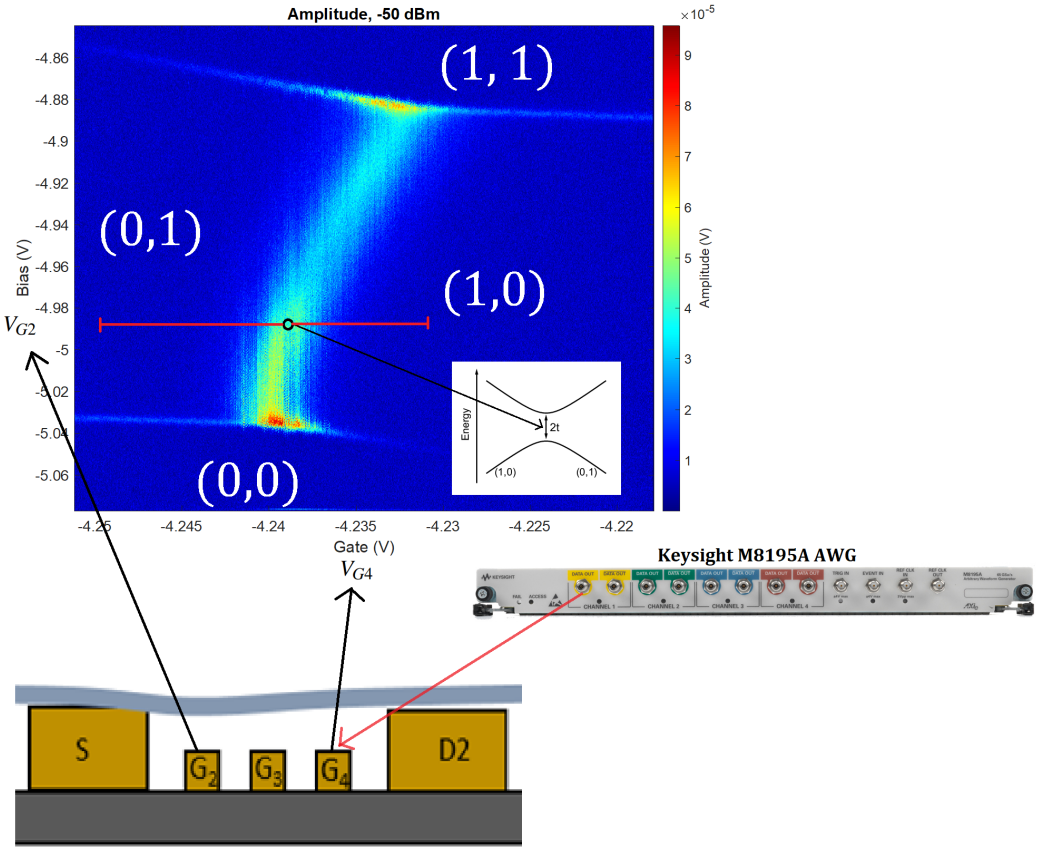

Figure 4.13: The high-level material model of the DQD with G_2 as the left (L) gate, G_4 as the right (R) gate, G_3 is fixed at the smallest tunnel coupling when at zero detuning. M8195A channel output 1 supplies gate G_4 at DC offset of -4.24 V. It should be noted these voltages undergo a series of attenuation and filters before reaching the DQD gates.

Shorter pulse widths (Rabi period) allow for faster operation times; desirable for faster qubit operations and a higher Q factor. The amplitude of the $\frac{\pi}{2}$ pulse determines how far into the Coulomb blockade region you move: Steps B and D in Fig. 4.14. A gate-voltage pulse of amplitude A_{MW} shifts the energy detuning $\varepsilon(t)$ between dots by an amount proportional to A_{MW}.

$$\varepsilon(t) = \varepsilon_0 + \kappa \cdot A_{MW} cos(w_d t) \tag{4.16}$$

Where κ is the lever arm converting gate voltage to detuning energy. At $\varepsilon = 0$, this modulation is purely transverse in the eigenbasis of $H = \frac{\varepsilon}{2}\sigma_z + t_c\sigma_x$, hence why

it drives transitions at zero detuning - it couples the ground and excited states directly.

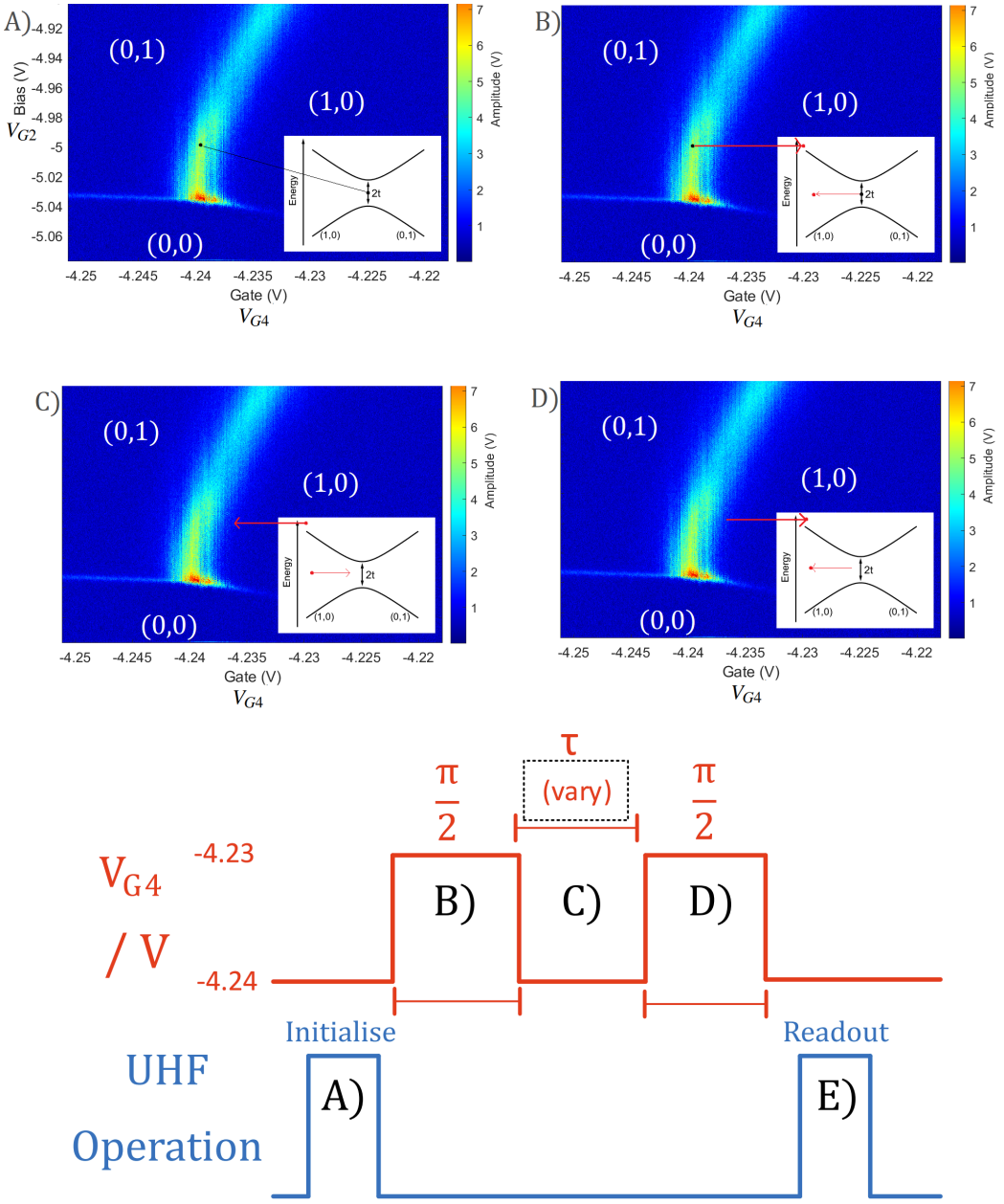

Figure 4.14: Ramsey control pulse scheme with MW drive to the right-dot, an example shown with a 1.148 GHz pulse and time delay τ which is varied. Each step in the pulse scheme is annotated as A), B), C), D) and E) to show the movement in stability and energy level detuning diagrams. UHF-LI operation signal (blue) shows when it is active A) and E), and in the wait state when low.

4.4 Summary of Charge State Measurements

- Developed a control framework for charge-qubit operations (Rabi/Ramsey style sequences) using synchronised microwave drive and gated reflectometry readout.
- Validated pulse synthesis, timing alignment, and demodulation using instrument-level loopback tests; confirmed the end-to-end response matches programmed frequency, phase, and envelope.
- Built simulation models establishing how to extract oscillation frequency and dephasing from time-domain traces.
- Assessed feasibility: with measured SNR–vs–integration and expected noise sources, estimated the parameter range (drive strength, detuning, integration time) where coherent oscillations and Ramsey fringes are resolvable.

4.5 Discussion and Results

This chapter explains how the applied microwave signal continuously to a gate-modulated DC signal excites the qubit predictably for further pulsed measurements, eventually to extract the dephasing time of the device. Using the Chapter 3 SNR curves, we find that sub-microsecond integration windows are realistic while retaining single-transition visibility, which keeps us in the regime where Rabi oscillations and Ramsey fringes should be resolvable for moderate tunnel couplings.

It is important to distinguish what has been demonstrated versus what is projected. The loopback tests confirm that our control stack can generate and read the signals required for qubit experiments; the simulations show how those signals would map to measured oscillations for plausible device parameters. The next step is execution on-device: calibrate detuning to energy using the lever arms, sweep drive power, and acquire time-domain datasets at fixed detuning to extract Rabi frequencies and T_2^*.

Chapter 5

Conclusion

This thesis presented a comprehensive study on the design and implementation of a control and readout toolbox for spin qubits in carbon nanotube-based Double Quantum Dot (DQD) systems. The work spanned instrumentation development, device measurement, and quantum control simulations for future Rabi oscillations and Ramsey interferometry experiments.

The project began with the integration and characterisation of advanced FPGA-based signal processing units from Zurich Instruments (UHF-QA and UHF-LI) and the Keysight M8195A Arbitrary Waveform Generator. Special emphasis was placed on achieving nanosecond-level synchronisation across these instruments through custom MATLAB drivers. These tools enabled coherent microwave control and fast feedback, which is critical for qubit pulse experiments. Characterisation of timing jitter, rise/fall time mismatches, and trigger latencies provided key insight into real-world pulse distortion and latency, enabling fine-tuning of the measurement protocol.

Reflectometry techniques were then applied to both Single and Double Quantum Dot devices. Early measurements of a single-dot shorted structure established the signal-to-noise performance of the system and informed the optimization of readout parameters. This was extended to DQD devices where Coulomb blockade and inter-dot transitions were mapped using 2D gate sweeps. The resulting charge-stability diagrams identified the operating conditions required to access the charge-qubit regime at zero-detuning, an optimal working point for coherent microwave

experiments.

Charge-qubit spectroscopy was then performed to identify resonance frequencies and tune tunnel coupling. This calibration enabled the implementation of pulsed microwave control, beginning with Rabi oscillation experiments. A QuTiP-based simulation of Rabi dynamics was developed and used to interpret the resulting oscillatory patterns, with extracted Rabi frequencies matched against known drive amplitudes and tunnel coupling values. The experimental sequences were performed using Gaussian-modulated pulses, and readouts were demodulated in real-time using the UHF-QA. These experiments validated the coherent oscillation of the qubit between ground and excited states and demonstrated the importance of pulse amplitude, timing, and sequence averaging in extracting meaningful dynamics.

Based on Rabi results, a Ramsey interference sequence was implemented to probe the coherence time of the qubit. The Ramsey experiment used two $\frac{\pi}{2}$ pulses separated by a variable delay, allowing the observation of phase evolution and decoherence. Both simulation and experiment produced interference fringes that decayed exponentially, allowing extraction of the qubit's T_2^* time. These results provided direct insight into the decoherence mechanisms acting on the CNT charge-qubit system, including charge noise and device-level tunnel coupling variations.

From a technical perspective, this work demonstrated the feasibility of precision microwave control in a carbon nanotube platform and the compatibility of commercial instruments with the specific timing and calibration demands of quantum pulse sequences. The in-house software drivers and simulation codes developed as part of this project now form a reusable framework for further experiments, including spin echo or multiqubit operations.

In summary, this thesis contributes both technical infrastructure and physical insight into the control of spin qubits in DQDs. It provides a critical stepping stone towards more advanced qubit calibration routines, benchmarking protocols, and fidelity analysis. Moreover, it illustrates how simulations can inform experimental design, and how coherent manipulation depends sensitively on signal fidelity and device calibration. Future work could extend this toolbox to include two-qubit gates,

spin-photon interfaces, and real-time feedback protocols, all of which are necessary ingredients for fault-tolerant quantum computation. By refining the measurement pipeline and validating the CNT-DQD platform, this project supports the broader effort to scale solid-state quantum technologies into useful computing architectures.

Appendix A

Two-qubit derivation of a CNOT gate

The NOT gate is another example gate operator, such as an identity gate, with two qubit inputs A and B. Firstly, the operator NOT for a single qubit B is:

$$NOT^{(B)} = |0\rangle_B \, {}^B\langle 1| + |1\rangle_B \, {}^B\langle 0| \tag{A.1}$$

Secondly, we consider when both qubits are in one of the Bell states and the NOT operator on qubit B $NOT^{(B)}$ becomes:

$$\begin{aligned} NOT^{(B)} \frac{1}{\sqrt{2}}(|00\rangle_{AB} + |11\rangle_{AB}) &= (|0\rangle_B \, {}^B\langle 1| + |1\rangle_B \, {}^B\langle 0|) \frac{1}{\sqrt{2}}(|00\rangle_{AB} + |11\rangle_{AB}) \\ &= \frac{1}{\sqrt{2}}(|01\rangle_{AB} + |10\rangle_{AB}) \end{aligned} \tag{A.2}$$

Likewise, the same operations can be shown and proven in the NOT gate matrix format, alternatively to eq. A.1, in matrices:

$$NOT^{(B)} = \begin{pmatrix} 0 & 1 & 0 & 0 \\ 1 & 0 & 0 & 0 \\ 0 & 0 & 0 & 1 \\ 0 & 0 & 1 & 0 \end{pmatrix} \tag{A.3}$$

The resulting expressions from equations A.4 and A.2 are:

$$
\begin{aligned}
NOT^{(B)}\frac{1}{\sqrt{2}}(|00\rangle_{AB}+|11\rangle_{AB}) &= \begin{pmatrix} 0 & 1 & 0 & 0 \\ 1 & 0 & 0 & 0 \\ 0 & 0 & 0 & 1 \\ 0 & 0 & 1 & 0 \end{pmatrix} \times \frac{1}{\sqrt{2}}\left(\begin{pmatrix} 1 \\ 0 \\ 0 \\ 0 \end{pmatrix} + \begin{pmatrix} 0 \\ 0 \\ 0 \\ 1 \end{pmatrix}\right) \\
&= \frac{1}{\sqrt{2}}\left(\begin{pmatrix} 0 \\ 1 \\ 0 \\ 0 \end{pmatrix} + \begin{pmatrix} 0 \\ 0 \\ 1 \\ 0 \end{pmatrix}\right)
\end{aligned}
\tag{A.4}
$$

Appendix B

Dilution Fridge setup

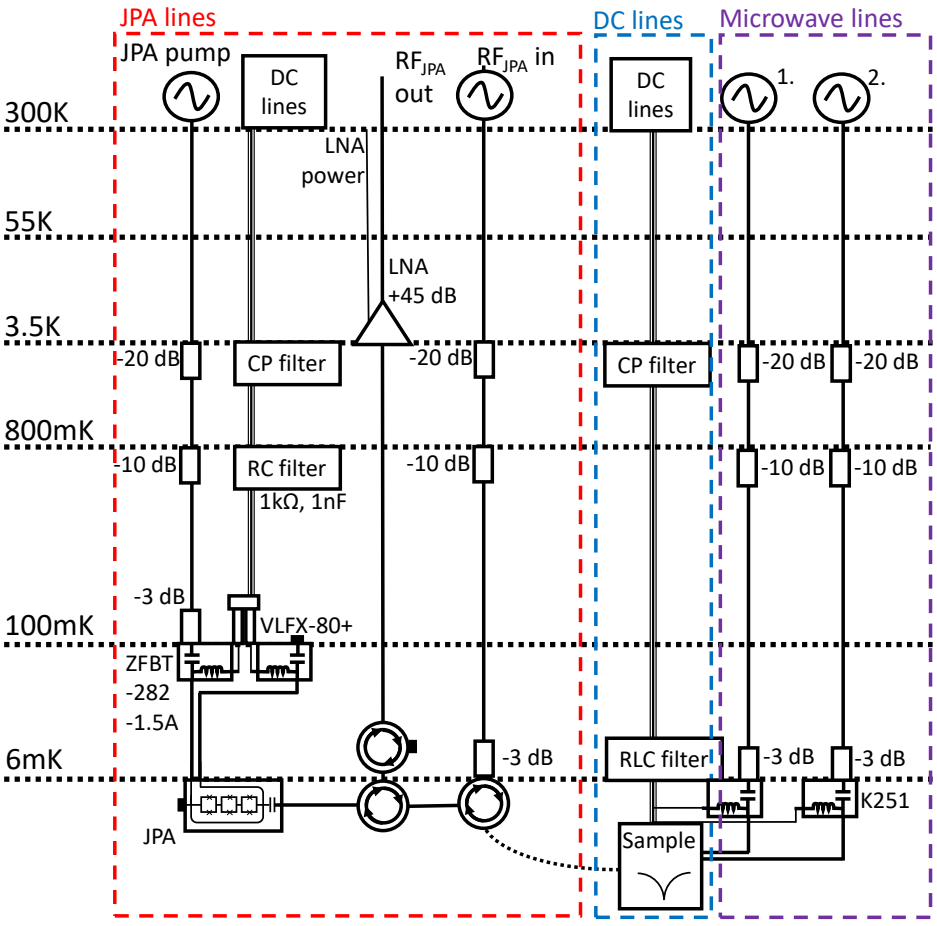

Figure B.1: Wiring Setup of the BlueFors LD-250 dilution fridge with dashed lineboxes highlighting the main wirings for JPA lines (red), DC lines (blue), and Microwave lines (Purple) at each temperature stage. The Quantum Dot sample is placed at the 6 mK mixing stage.

Bibliography

[1] Michael A. Nielsen and Isaac L. Chuang. *Quantum Computation and Quantum Information*. Cambridge University Press, 6 2012.

[2] Mark Buitelaar. Quantum Dots & Wires - Quantum Transport Lecture Notes, 2017.

[3] Maryam Elia, Noor Al-Hasi, and Wala Al-Tamimi. Introduction to quantum dots definition and applications. 10 2022.

[4] Zurich Instruments. UHFLI User Manual. Technical report, Zurich Instruments, 2023.

[5] Zurich Instruments. UHFQA User Manual. Technical report, 2023.

[6] Keysight Technologies. User's Guide Keysight M8195A Arbitrary Waveform Generator Revision 2. Technical report, 2019.

[7] Agilent. Signal Analysis Evolutions Overview : Types of Measurements.

[8] Keysight Technologies. Reference Guide K e y s i g h t Fundamentals of Arbitrary Waveform Generation A high performance AWG primer. Technical report, 2015.

[9] Paul Benioff. The computer as a physical system: A microscopic quantum mechanical Hamiltonian model of computers as represented by Turing machines. *Journal of Statistical Physics*, 22(5):563–591, 5 1980.

[10] Richard P. Feynman. Simulating physics with computers. *International Journal of Theoretical Physics*, 21(6-7):467–488, 6 1982.

[11] David Deutsch. Quantum theory, the Church–Turing principle and the universal quantum computer. *Proceedings of the Royal Society of London. A. Mathematical and Physical Sciences*, 400(1818):97–117, 7 1985.

[12] Peter W. Shor. Algorithms for quantum computation: Discrete logarithms and factoring. In *Proceedings - Annual IEEE Symposium on Foundations of Computer Science, FOCS*, pages 124–134. IEEE Computer Society, 1994.

[13] T. D. Ladd, F. Jelezko, R. Laflamme, Y. Nakamura, C. Monroe, and J. L. O'Brien. Quantum computers. *Nature*, 464(7285):45–53, 3 2010.

[14] E. Knill, R. Laflamme, H. Barnum, D. Dalvit, J. Dziarmaga, J. Gubernatis, L. Gurvits, G. Ortiz, L. Viola, and W. H. Zurek. Introduction to Quantum Information Processing. 7 2002.

[15] Grabert H. *Single Charge Tunneling*, volume 294. Springer US, Boston, MA, 1992.

[16] M. A. Kastner. The single-electron transistor. *Reviews of Modern Physics*, 64(3):849–858, 7 1992.

[17] L P Kouwenhoven, D G Austing, and S Tarucha. Few-electron quantum dots. *Reports on Progress in Physics*, 64(6):701–736, 6 2001.

[18] R. Hanson, L. P. Kouwenhoven, J. R. Petta, S. Tarucha, and L. M. K. Vandersypen. Spins in few-electron quantum dots. *Reviews of Modern Physics*, 79(4):1217–1265, 10 2007.

[19] J. R. Petta, A. C. Johnson, J. M. Taylor, E. A. Laird, A. Yacoby, M. D. Lukin, C. M. Marcus, M. P. Hanson, and A. C. Gossard. Coherent Manipulation of Coupled Electron Spins in Semiconductor Quantum Dots. *Science*, 309(5744):2180–2184, 9 2005.

[20] F. H. L. Koppens, C. Buizert, K. J. Tielrooij, I. T. Vink, K. C. Nowack, T. Meunier, L. P. Kouwenhoven, and L. M. K. Vandersypen. Driven coherent oscilla-

tions of a single electron spin in a quantum dot. *Nature*, 442(7104):766–771, 8 2006.

[21] K. C. Nowack, F. H. L. Koppens, Yu. V. Nazarov, and L. M. K. Vandersypen. Coherent Control of a Single Electron Spin with Electric Fields. *Science*, 318(5855):1430–1433, 11 2007.

[22] J. Yoneda, T. Otsuka, T. Nakajima, T. Takakura, T. Obata, M. Pioro-Ladrière, H. Lu, C. J. Palmstrøm, A. C. Gossard, and S. Z. Tarucha. Fast electrical control of single electron spins in Quantum dots with vanishing influence from nuclear spins. *Physical Review Letters*, 113(26), 12 2014.

[23] Kenta Takeda, Jun Kamioka, Tomohiro Otsuka, Jun Yoneda, Takashi Nakajima, Matthieu R. Delbecq, Shinichi Amaha, Giles Allison, Tetsuo Kodera, Shunri Oda, and Seigo Tarucha. A fault-tolerant addressable spin qubit in a natural silicon quantum dot. *Science Advances*, 2(8):e1600694, 8 2016.

[24] J. Raftery, A. Vrajitoarea, G. Zhang, Z. Leng, S. J. Srinivasan, and A. A. Houck. Direct digital synthesis of microwave waveforms for quantum computing. *arXiv*, pages 1–6, 2017.

[25] T. Hayashi, T. Fujisawa, H. D. Cheong, Y. H. Jeong, and Y. Hirayama. Coherent manipulation of electronic states in a double quantum dot. *Physical Review Letters*, 91(22), 2003.

[26] J. R. Petta, A. C. Johnson, C. M. Marcus, M. P. Hanson, and A. C. Gossard. Manipulation of a Single Charge in a Double Quantum Dot. *Physical Review Letters*, 93(18):186802, 10 2004.

[27] E. A. Laird, F. Pei, and L. P. Kouwenhoven. A valley–spin qubit in a carbon nanotube. *Nature Nanotechnology*, 8(8):565–568, 8 2013.

[28] S Nadj-Perge, S M Frolov, E P A M Bakkers, and L P Kouwenhoven. Spin-orbit qubit in a semiconductor nanowire. *Nature*, 468(7327):1084–7, 12 2010.

[29] F. H.L. Koppens, K. C. Nowack, and L. M.K. Vandersypen. Spin echo of a single electron spin in a quantum dot. *Physical Review Letters*, 100(23), 6 2008.

[30] E. Paladino, Y.M. Galperin, G. Falci, and B.L. Altshuler. / noise: Implications for solid-state quantum information. *Reviews of Modern Physics*, 86(2):361–418, 4 2014.

[31] J. Medford, Ł. Cywiński, C. Barthel, C. M. Marcus, M. P. Hanson, and A. C. Gossard. Scaling of Dynamical Decoupling for Spin Qubits. *Physical Review Letters*, 108(8):086802, 2 2012.

[32] Andrew F. May, Stuart Calder, Claudia Cantoni, Huibo Cao, and Michael A. McGuire. Magnetic structure and phase stability of the van der Waals bonded ferromagnet ¡math¿ ¡mrow¿ ¡msub¿ ¡mi¿Fe¡/mi¿ ¡mrow¿ ¡mn¿3¡/mn¿ ¡mo¿¡/mo¿ ¡mi¿x¡/mi¿ ¡/mrow¿ ¡/msub¿ ¡msub¿ ¡mi¿GeTe¡/mi¿ ¡mn¿2¡/mn¿ ¡/msub¿ ¡/mrow¿ ¡/math¿. *Physical Review B*, 93(1):014411, 1 2016.

[33] Mason J. Gray, Josef Freudenstein, Shu Yang F. Zhao, Ryan O'Connor, Samuel Jenkins, Narendra Kumar, Marcel Hoek, Abigail Kopec, Soonsang Huh, Takashi Taniguchi, Kenji Watanabe, Ruidan Zhong, Changyoung Kim, G. D. Gu, and K. S. Burch. Evidence for Helical Hinge Zero Modes in an Fe-Based Superconductor. *Nano Letters*, 19(8):4890–4896, 8 2019.

[34] Marc Bockrath, David H. Cobden, Paul L. McEuen, Nasreen G. Chopra, A. Zettl, Andreas Thess, and R. E. Smalley. Single-Electron Transport in Ropes of Carbon Nanotubes. *Science*, 275(5308):1922–1925, 3 1997.

[35] E. D. Minot, Yuval Yaish, Vera Sazonova, and Paul L. McEuen. Determination of electron orbital magnetic moments in carbon nanotubes. *Nature*, 428(6982):536–539, 4 2004.

[36] F. Kuemmeth, S. Ilani, D. C. Ralph, and P. L. McEuen. Coupling of spin and orbital motion of electrons in carbon nanotubes. *Nature*, 452(7186):448–452, 3 2008.

[37] G. A. Steele, G. Gotz, and L. P. Kouwenhoven. Tunable few-electron double quantum dots and Klein tunnelling in ultraclean carbon nanotubes. *Nature Nanotechnology*, 4(6):363–367, 6 2009.

[38] J. Flipse, F. L. Bakker, A. Slachter, F. K. Dejene, and B. J. van Wees. Direct observation of the spin-dependent Peltier effect. *Nature Nanotechnology*, 7(3):166–168, 3 2012.

[39] J. J. Viennot, M. C. Dartiailh, A. Cottet, and T. Kontos. Coherent coupling of a single spin to microwave cavity photons. *Science*, 349(6246):408–411, 7 2015.

[40] S. L. N. Hermans, M. Pompili, H. K. C. Beukers, S. Baier, J. Borregaard, and R. Hanson. Qubit teleportation between non-neighbouring nodes in a quantum network. *Nature*, 605(7911):663–668, 5 2022.

[41] K. D. Petersson, C. G. Smith, D. Anderson, P. Atkinson, G. A.C. Jones, and D. A. Ritchie. Charge and spin state readout of a double quantum dot coupled to a resonator. *Nano Letters*, 10(8):2789–2793, 8 2010.

[42] Visa Vesterinen, Olli-Pentti Saira, Ilmo Räisänen, Mikko Möttönen, Leif Grönberg, Jukka Pekola, and Juha Hassel. Lumped-element Josephson parametric amplifier at 650 MHz for nano-calorimeter readout. *Superconductor Science and Technology*, 30(8):085001, 8 2017.

[43] Melvin Lax, Wei Cai, Min Xu, Melvin Lax, Wei Cai, and Min Xu. Thermal noise. *Random Processes in Physics and Finance*, pages 82–92, 2010.

[44] Jun Yoneda, Kenta Takeda, Tomohiro Otsuka, Takashi Nakajima, Matthieu R. Delbecq, Giles Allison, Takumu Honda, Tetsuo Kodera, Shunri Oda, Yusuke Hoshi, Noritaka Usami, Kohei M. Itoh, and Seigo Tarucha. A quantum-dot spin qubit with coherence limited by charge noise and fidelity higher than 99.9%. *Nature Nanotechnology*, 13(2):102–106, 2018.

[45] Qiskit. https://qiskit-community.github.io/qiskit-dynamics/tutorials/Rabi_oscillations.html, 2020.

[46] T. F. Watson, S. G. J. Philips, E. Kawakami, D. R. Ward, P. Scarlino, M. Veldhorst, D. E. Savage, M. G. Lagally, Mark Friesen, S. N. Coppersmith, M. A. Eriksson, and L. M. K. Vandersypen. A programmable two-qubit quantum processor in silicon. *Nature*, 555(7698):633–637, 3 2018.

[47] I. Khanonkin, A. K. Mishra, O. Karni, S. Banyoudeh, F. Schnabel, V. Sichkovskyi, V. Mikhelashvili, J. P. Reithmaier, and G. Eisenstein. Ramsey fringes in a roomerature quantum-dot semiconductor optical amplifier. *Physical Review B*, 97(24), 6 2018.

[48] Z. V. Penfold-Fitch, F. Sfigakis, and M. R. Buitelaar. Microwave Spectroscopy of a Carbon Nanotube Charge Qubit. *Physical Review Applied*, 7(5), 5 2017.